Oncogenic *RAS* instructs morphological transformation of human epithelia via differential tissue mechanics.

Authors
A. Nyga[1,2], J. Muñoz[3], S. Dercksen[4], G. Fornabaio[1,5], M. Uroz[1], X. Trepat[1,6,7,8], B. Baum[2,9], H. Matthews[9], V. Conte[1,4,10,*]

Affiliations

[1] Institute for Bioengineering of Catalonia (IBEC), The Barcelona Institute of Science and Technology (BIST), Barcelona – Spain

[2] MRC Laboratory of Molecular Biology, Cambridge – United Kingdom

[3] Department of Mathematics, Polytechnic University of Catalonia (UPC), Barcelona – Spain

[4] Department of Biomedical Engineering, Eindhoven University of Technology (TU/e), Eindhoven – the Netherlands

[5] Department of Physics, University of Barcelona (UB), Barcelona - Spain

[6] Centro de Investigación Biomédica en Red en Bioingeniería, Biomateriales y Nanomedicina (CIBER-BBN), Barcelona – Spain

[7] Department of Biomedicine, University of Barcelona (UB), Barcelona – Spain

[8] Institució Catalana de Recerca i Estudis Avançats (ICREA), Barcelona – Spain

[9] MRC Laboratory of Molecular Cell Biology, University College London (UCL), London – United Kingdom

[10] Institute for Complex Molecular Systems (ICMS), Eindhoven University of Technology (TU/e), Eindhoven – the Netherlands
* Corresponding author: v.conte@tue.nl

Abstract
The loss of epithelial homeostasis and the disruption of normal tissue morphology is a hallmark of tumor development. Here, we ask how the uniform activation of an oncogene, *RAS*, impacts the morphology and tissue mechanics in a normal epithelium. We found that inducible induction of *HRAS* in confined epithelial monolayers on soft substrates drives a morphological transformation of a 2D monolayer into a compact 3D cell aggregate. This transformation was initiated by the loss of monolayer integrity and formation of two distinct cell layers with differential cell-cell junctions, cell-substrate adhesion, and tensional states. Computational modelling revealed how adhesion and active peripheral tension induces inherent mechanical instability in the system, which drives the 2D to 3D morphological transformation. Consistent with this, removal of epithelial tension through the inhibition of acto-myosin contractility halted the process. These findings reveal the mechanisms by which oncogene activation within an epithelium can induce mechanical instability to drive morphological tissue transformation.

Introduction

Epithelia are layered tissues, which provide separation between the inside (the stroma) and external environment. To perform this barrier function, the morphology of the epithelial tissues must be maintained as individual cells proliferate and die. Maintenance of epithelial homeostasis requires control of cell density through the dynamic regulation of cell proliferation, cell packing (*1*) and cell extrusion (*2–4*); the maintenance of a sheet-like morphology through the tight cell-cell association, through intercellular junctions (*5*) and stable anchoring between cells and the extracellular matrix (*6*).

Loss of homeostasis and the subsequent breakdown of tissue organization is a hallmark of epithelial-derived cancers, where oncogene activation results in the loss of carefully balanced control mechanisms. *RAS* oncogenes (*HRAS*, *NRAS* and *KRAS*) are one of the most common mutated genes in human cancer with *RAS* activation occurring in around 30% of all cancers (*7, 8*). *RAS* activation impacts individual cell mechanics through alterations in acto-myosin contractility (*9–12*). At the tissue scale, *RAS* disrupts epithelial homeostasis resulting in loss of tissue polarity(*13*) and barrier function (*14*). Normal epithelia act as a barrier against single *RAS* cells or *RAS* cell clusters through their extrusion or delamination (*15–21*). Extrusion is regulated through differential tissue tension between normal and transformed cells (*20*, *22*) and can be impacted by tissue-level mechanical forces (*23*). Larger clusters of *RAS* cells can separate from normal neighbors (*24*, *25*) to form cysts (*19*), outgrowths or invaginations (*26*). Despite these morphological and mechanical roles for *RAS*, it is still not clear how cell and tissue mechanics mediate *RAS*-signaling to morph epithelia independently of interactions between non-transformed and *RAS*-transformed cells.

Here we investigated how the uniform activation of oncogenic *RAS* alters the morphology and mechanics of an epithelial monolayer as well as their crosstalk. We inducibly activated *HRAS* in confined normal epithelial monolayers grown on soft physiological substrates. We found that oncogenic *HRAS* expression was sufficient to induce the transition of an epithelial monolayer into a multi-layered structure characterized by layer-specific differences in cell-cell contractility and cell-matrix adhesions. This transitory state of mechanical instability sets the epithelia on a path to a 3D morphological transformation driven by an increase in peripheral tension.

Results

Oncogenic *RAS*-expression induces the active dewetting of confined MCF10A monolayers

To systematically study the effects of *RAS*-activation on epithelial morphology and mechanics live (Fig. 1 A), we conditionally activated oncogenic *HRAS* in non-transformed MCF10A human epithelial cells – MCF10A/ER:HRAS^{V12}(*27*). We emulated the physiological stiffness of basement membrane and underlying ECM by plating cells on soft polyacrylamide-gel substrates with a stiffness of 12 kPa(*28, 29*). We coated substrates with rat tail collagen type-I micropatterned in circular shapes of 400 μm in diameter (Fig. 1 A). Epithelial cells were grown on these soft circular micropatterned substrates for 24 hours. At the time point t = 0 hours the expression of *HRAS.V12* was induced in the epithelial monolayers through the addition of 4-OHT (*HRAS*-transformed epithelia) – at the same time point, vehicle control (DMSO) was added to the remaining cellular monolayers for control (non-transformed epithelia). Surprisingly, we found that HRAS activation (Fig. 1B) was sufficient to transform the 2D epithelial monolayer into a 3D mass (Fig. 1 C-D and Fig. S1).

To define the path of this 2D-to-3D cellular transformation, we monitored the process via a set of objective morphological (Fig. 1) and mechanical measures (Fig. 2). Specifically, we quantified the area (Fig. 1 E), aspect ratio (Fig. 1 G), circularity (Fig. 1 H) and traction forces (Fig. 2) for each cellular island.

Morphological analyses revealed differences between RAS and control epithelial monolayers beginning ~4 hours after *HRAS* induction. Whereas control monolayers remained flat and maintained a near constant area throughout the time window of our analysis, from 4 hours after oncogenic *HRAS* induction, monolayer islands exhibited a slow decrease in area. This decrease in circular area continued in an approximately symmetric fashion up until 24 hours after *HRAS* induction, after which the symmetry of *HRAS*-transformed islands started to break (Fig. 1 E-H). At this point, *HRAS*-transformed monolayers underwent a loss of circularity and an increase in aspect ratio (Fig. 1 G-H). This was followed by a rapid transition as the 2D *HRAS*-transformed epithelium started to morph into a 3D cell mass (Fig. S1). None of these changes were seen in control non-transformed monolayers. To study the impact of cell proliferation induced by *HRAS*, we compared number of cells in *HRAS*-transformed epithelia at 12 hours with number of cells in non-transformed epithelia over the span of the time window of our analysis – at 12 hours *RAS*-transformed epithelia were still monolayers and their area had started decreasing significantly compared to pre-transformation levels. By contrast a steady increase in number of cells of non-transformed epithelia was not accompanied by a significant decrease in surface area compared to pre-transformation levels (Fig. 1 I). Additionally, we inhibited cell proliferation by arresting the cell cycle (RO-3306, Fig. 1 J), and still observed 2D *RAS*-transformed monolayers morphing into a 3D cell mass (Fig. 1 J). Taken together, these results indicated that cell proliferation did not drive the 2D-to-3D morphological transition undergone by *HRAS*-transformed monolayers.

Mechanical analyses carried out using Traction Force Microscopy(*30*) showed that traction forces of higher magnitude were mainly localized at the periphery of both non-transformed and *HRAS*-transformed epithelial monolayers (Fig. 2 A, F-G). In both cases, the elastic strain energy actively transferred by the epithelium to the underlying substrate also followed a similar trend (Fig. S2). The concentration of traction force at the periphery of circular epithelia is in line with previous theoretical(*31, 32*) and experimental studies carried out on epithelial colonies of human colon carcinoma (HCT-8)(*33*) and on confined circular monolayers of canine kidney cells (MDCK)(*34, 35*).

We noticed that high traction forces tended to be more ordered at the epithelium's periphery (Fig. 2 A,B). In order to decompose the traction field along the directions normal and tangential to the epithelial domain's edge (Fig. S3), we computed: i) the net radial ($T_\perp$) and net tangential ($T_\parallel$) traction force components as a function of time in the whole epithelial domain as well as in the central (inner) and peripheral (outer) domains (Fig. 2 E). These time-trends (Fig. 2 H-K) confirmed that the net physical interactions at the interface between epithelia and substrate developed along the direction perpendicular to the epithelium's edge for both non-transformed and *HRAS*-transformed epithelia throughout the analysis.

To further average out spatial-temporal fluctuations of the traction force field and to better visualize reproducible force patterns, we averaged the net radial traction components $T_\perp$ in space, along lines concentric to the edge of the island. Upon displaying these space-averages as a function of distance from the epithelial domain's edge, we obtained kymographs of the net radial traction component $T_\perp$ for both non-transformed (Fig. 2 L) and *HRAS*-transformed MCF10A epithelia (Fig. 2 M). Kymographs confirm that it is the intense net radial-traction components that concentrate mainly at the periphery of both non-transformed and *HRAS*-transformed epithelia throughout the experiment. By analyzing the stress distribution within the epithelial domain through Monolayer Stress Microscopy(*30*) (Materials&Methods), we further showed that non-transformed epithelia successfully establish and maintain epithelial homeostasis by means of long-range transmission of physical forces throughout the monolayer from opposite locations of the epithelial domain's edge, which results in tension accumulating throughout the bulk of the epithelial domain (Fig. S4).

Our traction force analysis also showed that, unlike control epithelia, the average intensity of the traction field of *HRAS*-transformed epithelia undergoes a characteristic two-phase oscillation in the time window of our analysis (Fig. 2 G). This was observed as a decreasing-increasing phase over the first 24 hours following *HRAS* induction – when average traction forces dropped for approximately 8 hours before recovering again by approximately 24 hours (Fig. 2 G-I). This disrupts the mechanical homeostasis of intact non-transformed circular epithelia and sets them on course of an abrupt symmetric decrease in epithelial area within the first 24 hours of oncogene activation (Fig. 1 E) followed by a 2D-to-3D morphological transformation (Fig. 1 B and Fig. S1).

As expected, the overexpression of $KRAS^{V12}$ in confined circular epithelia respectively led to similar results. Upon $KRAS^{V12}$-activation, confined circular monolayers of inducible MCF10A/ER:$KRAS^{V12}$ cells followed a similar morpho-mechanical fate to those of MCF10A/ER:$HRAS^{V12}$ cells, suggesting that different RAS isoforms *HRAS* and *KRAS* have similar morpho-mechanical effects (Fig. S5).

The relatively rapid morphological (Fig. 1) and mechanical (Fig. 2) changes observed in confined transformed MCF10A monolayers from t=24 hours onward are reminiscent of previously described cellular process of active dewetting(*36*), in which the tissue retraction is driven by a monotonical increase in tension and in cell-matrix traction forces oriented towards the center of the circular monolayer. Thus, having observed a 2D-to-3D transition following *RAS* activation we hypothesized that oncogenic *RAS* expression primes epithelia for dewetting in the first 24 hours of *RAS* expression by inducing structural and mechanical changes within the monolayer while still morphologically flat. To test this, we turned our focus to the changes in epithelial organization during the first 24 hours of cellular evolution from *RAS*-activation.

Oncogenic *HRAS* expression triggers the bilayering of confined MCF10A monolayers

By analyzing cellular deformations in the z-plane orthogonal to the underlying substrate, we observed early changes in both nuclear and monolayer height (Fig. 3 A-B). Thus, within 24 hours of oncogene activation *RAS*-transformed epithelia became an average of 25% thicker than non-transformed ones (Fig. 3 A and Fig. S6). This was accompanied by an increase in cell packing that was markedly higher in the confined *RAS*-transformed monolayers, leading to the observed decrease in the area of individual cells (Fig. 3 C). The heights of nuclei in both non-transformed and *RAS*-transformed MCF10A monolayers were uniform up to 8 hours from oncogene activation (Fig. 3 B). Thereafter and up until 24 hours, the heights of nuclei of *RAS*-transformed epithelia showed greater heterogeneity, an indicator of the presence of topological heterogeneities within the confined epithelium(*37*). Indeed, the *RAS*-expressing epithelium (but not the control) became multi-layered over this time period (Fig. 3 D). Confocal microscopy revealed how confined *RAS*-transformed epithelia segregated into two discrete cellular layers with very distinct organizations (Fig. 3 D-E). The cells forming the top layer of *RAS*-transformed epithelia were flatter and more spread than those in the bottom layer (Fig. 3 E), having undergone a 1.5-fold increase in cell perimeter (Fig. 3 G) and a 3-fold average increase in the cell area (Fig. 3 F) without any substantial effect on cell shape – the cell aspect ratio remained approximately constant in both layers (Fig. 3 H). We next turned our focus on the cellular alterations that could cause the bilayering.

Oncogenic *HRAS*-expression induces layer-specific differences in cell-cell contractility and cell-matrix adhesions of the confined MCF10A bilayers.

Stable RAS transformation has been shown to disrupt cadherins to promote cell invasion(*38–40*). Therefore, we hypothesized that the bilayering induced by oncogenic *RAS*-expression might also be caused by disruption to cell-cell junctions. Non-transformed MCF10A cells constitutively expressed E-cadherin and, thus, exhibited uniform cell-cell junctions throughout the epithelium.

Strikingly, E-cadherin expression did not change during *RAS*-activation (Fig. 4 A). Nevertheless, we observed differences in the localization of E-cadherin in the two layers of the developing bilayer (Fig. 4 B). Cells in the bottom layer tended to have relatively low levels of E-Cadherin at cell-cell junctions, while junctional E-cadherin levels remained similar to those before *RAS* activation in the top layer (Fig. 4 C). In addition, the ratio of junctional to cytoplasmic E-cadherin was decreased in the bottom layer (Fig. 4 D), suggestive of a redistribution of the protein from junctions to cytoplasm. Intriguingly, this change in E-cadherin localization in the bottom layer induced by the *RAS*-transformation was paralleled by a reduction of cell-matrix adhesion between the epithelial cells of this layer and the hydrogel substrate, as shown by a decrease in the expression of the collagen receptor integrin β1 (Fig. 4 E-G).

The structural alterations occurring in *RAS*-transformed epithelia at the level of cell-cell junctions (Fig. 4 A-E) and cell-matrix adhesions (Fig. 4 E-G) correlated with the initial decrease observed in traction forces transferred by the epithelium to the substrate matrix during the first ~8 hours of oncogene induction (Fig. 2 G). However, traction forces recovered to pre-transformation levels by 24 hours of *RAS*-transformation (Fig. 2 G), while adhesion to the substrate kept decreasing without recovering (Fig. 4 E-G). Therefore, we hypothesized that active tension within the epithelium might also be affected by the *RAS*-transformation. To further understand whether *RAS*-driven alterations to epithelial structure are reflected in changes in epithelial tension (driven by the contractile cellular actomyosin cortex(*41*, *42*)), we studied the distribution of key cortex components F-actin and pMLC2(*43*) in both non-transformed and *RAS*-transformed epithelia. While non-transformed epithelia show uniform distribution of F-actin and pMLC2 (Fig. 5 A-C), oncogenic *RAS* expression induced a gradient in the distribution of F-actin and pMLC2 throughout the bilayer within 24 hours of oncogene activation (Fig. 5 D-H). F-actin and pMLC2 fluorescent intensity were higher at the periphery of the bottom layer of *RAS*-transformed bilayers (Fig. 5 D-F). This fluorescent intensity was lower and more heterogeneously distributed throughout the top layer (Fig. 5 G-H), although spots of highly increased pMLC2 expression were visible at the periphery and in the middle of top layer of *RAS*-transformed bilayers (Fig. 5 G). Unexpectedly, these results show that while non-transformed monolayers retain a uniform homogenous state of tension (Fig. S4) and organization (Fig. 1-2) as they grow under these conditions, the uniform expression of oncogenic *RAS* for 24 hours leads to the establishment of a tension gradient that destabilizes the epithelium. Thus, *RAS*-transformed circular epithelia underwent a significant radially symmetric contraction (Fig. 1, E-I) and formed multiple layers with very different properties (Fig. 2). We hypothesized that these *RAS*-induced alterations to cell-cell junctions, cell-matrix junctions, and epithelial tension prime the bilayers for active dewetting. To test whether this is likely to be the case, we developed a simple computational model of circular cellular monolayer.

Oncogenic *HRAS*-expression makes confined monolayers mechanically instable

The *RAS*-transformed circular epithelial bilayers were modelled *in silico* as a 2D continuum elastic disk having finite thickness in approximation of plain-stress (Fig. 6 A, Materials & Methods). The epithelial disk was mechanically coupled to the substrate matrix at discrete focal contact points (Fig. 6 B). The effects of *RAS*-induction were modelled based on experimental data (Materials & Methods). The model emulated the dynamics of discrete focal contact points between cells of the monolayer and the substrate matrix by means of a viscoelastic solid friction law (*44*). Decreased adhesion between *RAS*-transformed bilayers and the underlying substrate matrix (Fig. 4 F-G) was emulated in the model by a uniform value of solid friction that decreases in time (Fig. 6F – Materials & Methods). Increased cellular tension at the periphery of *RAS*-transformed bilayers, as observed in the experimental distributions of F-actin and pMLC2 (Fig. 5 C,F) was emulated in the model by an increase in contractility (Fig. 6 G) at the epithelial disk's periphery (Fig. 6 G). Increase in tension intensity was made proportional to the relative

fluorescence intensities of pMLC2 (Fig. 5 C, Materials & Methods). The finite element method was used to numerically resolve the bilayer's deformations generated by active contractile cellular forces against friction of the *in silico* epithelial disk with the substrate (Fig. 6 C-D, Materials & Methods). We then computed the profiles of the area of the epithelial disk and the traction force transmitted to the substrate (Fig. 6 H-M) as a function of cellular contractility (Fig. 6 G) and/or cell-matrix adhesion (Fig. 6 F).

Our simulations confirmed that an initial decrease in the adhesion between the epithelial disk and the underlying matrix resulted in a decrease in average traction force magnitude (Fig. 6K) and early contraction of the epithelium (Fig. 6 H). However, despite cell-matrix adhesion further decreasing, our simulations showed that a progressive increase in epithelial tension led to the recovery of traction force magnitude to pre-transformation levels (Fig. 6 K) and further contraction of the epithelium (Fig. 6 H). This result physically validates that the timed combination of a decrease in cell-matrix adhesion and the increase in active epithelial tension of the types observed experimentally (Fig. 4 G and 5 C,F) is sufficient to emulate epithelial bilayer's retraction and the oscillation of the traction force magnitude to the extents observed in vitro (Fig. 1 E and Fig. 2 G,I). Our simulations shows that the reduction in cell-matrix adhesion alone could only account for a monotonical reduction in traction-force magnitude (Fig. 6 L) whereas the increase in cell-cell tension alone could only lead to a monotonical increase of traction-force magnitude (Fig. 6 M) and decrease in epithelial area (Fig. 6 L).

Taken together, our simulations and experiments suggested that *RAS*-transformation induced a state of mechanical instability in epithelia during the first 24 hours of oncogene induction, where increased cell-cell tension is unbalanced by decreased cell-matrix adhesion. As a result, the homeostatic equilibrium of the *RAS*-transformed bilayers is lost, and this sets the bilayers on a path to a 3D morphological transformation.

To further ascertain this thesis *in vitro*, we interfered with the build-up of epithelial tension at 6 hours (earlier stage, Fig. 7 B-C,F-G) and at 24 hours (later stage, Fig. 7 D-E,H-I) from *RAS* induction via pharmaceutical treatments of *RAS*-transformed epithelia (Fig. 7 A). The early reduction of epithelial tension via the inhibition of ROCK (Y27632, Fig. 7 A,B) or myosin II (Blebbistatin, Fig. 7 A,C) at 6 hours prevented traction forces from recovering to pre-transformation levels within 24 hours of oncogene activation (Fig. 7 F) preventing the contraction of epithelial monolayer (Fig. 7 G). The late reduction of epithelial tension via the inhibition of ROCK (Y27632, Fig. 7 A,B) or Myosin II (Blebbistatin, Fig. 7 A,C) at 24 hours caused drop in increasing traction forces (Fig. 7 H) and prevented the morphological dewetting of the *RAS*-transformed bilayers at later time points (Fig. 7 I). Hence, reduction of epithelial tension through ROCK or myosin II inhibition restored the mechanical stability of *RAS*-transformed epithelia within the time window of our analyses.

Discussion

The *RAS*-genes superfamily functions as a crucial signaling hub within the cell, which controls several of its critical signaling cascades. This also reflects how profoundly the abnormal activity of *RAS* affects human development and disease (*7, 8, 45*). *RAS* mutations alter the morphology and mechanics of individual cells (*46*), and here we showed how these morpho-mechanical changes can become integrated at the tissue scale to instruct the abnormal morphing of non-transformed MCF10A epithelia (Fig. 1). Here, we have used a combined experimental and computational analyses to ask how *RAS*-signaling instructs cell mechanics to alter the shape of epithelia. Our analysis showed, quite surprisingly, that uniform *RAS*-induction induced changes in cellular morphologies and forces affecting the homeostasis of intact confined MCF10A epithelial monolayers (Fig. 1,2), which ultimately led to the formation and contraction of a complex 3D cellular architecture via active dewetting (Fig. S1).

This morpho-mechanical transformation is mediated by a series of changes in epithelial architecture and mechanics that are induced during the first 24 hours of uniform *HRAS*-oncogene induction (Fig. 3). These include: i) the establishment of two layers of cells that have very different patterns of a E-cadherin localization, with high E-cadherin cell-cell junctions in the top layer and low E-cadherin cell-cell junctions in the bottom layer (Fig. 4); ii) local reductions in cellular adhesion to the substrate (Fig. 4), leading to decreased traction-forces transferred by the affected tissues to the substrate (Fig. 2); and, iii) a redistribution of regulators of cellular tension (F-actin and pMLC2), which become concentrated at the periphery of the bilayer (Fig. 5). In the future it will be fascinating to assess how these local changes in cell biology are induced by the uniform expression of oncogenic *RAS*. Our analysis shows how these local heterogeneities, when combined, give rise to the change in overall tissue organization and mechanics.

In a previous study, overexpression of E-cadherin in cancer cells set the epithelial monolayer for active dewetting (*36*). Here, we show that *HRAS* drives a decrease in cell-matrix adhesion and the redistribution of main regulators of epithelial tension, such as: i) F-actin and pMLC2, which became concentrated at the periphery of the bilayer (Fig. 5 C,F); and, ii) E-cadherin, which became differentially distributed between the top and bottom layers of the bilayer (Fig. 4 A-E). Our computational simulations validate that the imbalance in cell-cell tension and cell-matrix adhesion brought about by oncogenic *RAS*-expression is sufficient to place *RAS*-transformed epithelia into a state of mechanical instability (Fig. 6), which primes them for active dewetting (Fig. 1). Actively reducing tension through ROCK or myosin-II inhibition further validated the role of the mechanical instability in this morpho-mechanical process.

Taken together, our findings demonstrate how activation of *RAS* oncogenes, even over short time periods, induces a mechanical imbalance in epithelial monolayers that results in the loss of homeostasis and a dramatic morphological transformation mimicking those seen in *RAS*-mutant human tumors. In pancreatic cancer, mechanical imbalance following the oncogenic *KRAS*-expression drives the pathological morphing of the pancreatic duct (*26*). In squamous cell carcinoma, *HRAS* activation leads to layering via the loss of tissue polarity and organization (*47*). Here, we show that *RAS*-driven formation of two tissue layers with very different adhesive and contractile properties is a key event in the disruption of homeostatic equilibrium. Importantly, by establishing a mechanical imbalance through *RAS*-transformed tissues, epithelial bilayering may also provide a favorable intermediate mechanism to abnormally morph epithelia without the need for an extended interface with non-transformed tissues (*48, 19, 25, 26, 49*). Overall, our findings establish a new physical mechanism of cellular collectives through which *RAS* can regulate the pathological morphology of epithelia autonomously of cell competition.

Materials and Methods

Experimental design

To study mechanics in epithelial monolayers, we cultured epithelial cells on micropatterned polyacrylamide gels of defined stiffness (12 kPa). Detailed steps are described below.

MCF10A cell culture. Immortalized epithelial breast cell line MCF10A was transfected with inducible ^{12}V-mutated form of the *HRAS* gene (a gift from Julian Downwards lab UCL, London, UK)(*27*), referred to as MCF10A/ER.HRAS V12. They were maintained in complete medium composed of: phenol-free DMEM-F12 medium (ThermoFisher, #11039047) supplemented with 5% charcoal-stripped horse serum (ThermoFisher, #16050122), 100 U/ml penicillin and 100 µg/ml streptomycin (ThermoFisher, #15070), 20 ng/ml EGF (Peprotech, #AF100-15), 0.5 mg/ml hydrocortisone (Sigma, #H0888), 100 ng/ml cholera toxin (Sigma, #C8052) and 10 µg/ml insulin (Sigma, #I1882)(*50*), at 37°C in a humidified incubator with 5% CO_2. Confluent cells were passaged every 2/3 days at 1:4 dilution.

Polyacrylamide (PAA) gel substrates. Glass-bottom 6-well dishes (#0 thickness, IBL, #220.200.020) were treated with a bind-silane solution consisting of PlusOne Bind-Silane (VWR, #17-1330-01) and acetic acid (Pancreac Quimica, #131008-1612) in absolute ethanol for 1 hr at room temperature (RT) in a fume hood. Wells were washed 3 time with ethanol and dried. PAA gels with a Young's modulus of 12 kPa were prepared by mixing 18.8% of 40% w/v acrylamide (Bio-Rad, #1610140), 8% of 2% w/v bis-acrylamide (Bio-Rad, #1610142), 0.5% of 10% ammonium persulfate (APS, Bio-Rad, #161-0700), 0.05% of N,N,N,N'-tetramethylethylenediamine (TEMED, Sigma Aldrich, #T9281), 0.7% of FluoSpheres carboxylate modified microspheres (0.2µm, dark red, ThermoFisher, #F8807) in HEPES solution (ThermoFisher, #15630056). 22 µl of solution was placed on the treated glass well and covered with 18 mm diameter coverslip. After 1hr polymerization at RT, PBS was added to the wells and coverslips were carefully removed. Gels were washed with PBS.

Polydimethylsiloxane (PDMS) membranes. SU8-50 master containing circular patterns of 400 µm diameter and 50 µm height was prepared using conventional photolithography. PDMS was spin-coated on the masters to a thickness lower than the height of the SU8 features (15 µm) and cured overnight at 85°C. A thick border of PDMS was left at the edges of the membranes for the handling purpose. PDMS membranes were peeled off and kept at 4°C until use.

Collagen patterning. To pattern collagen on top of PAA gels, gels were functionalized with a solution of 1mg/ml Sulfo-SANPAH (sulfosuccunimidyl 6-(4'-azido-2'-nitrophenylamino) hexanoate, ThermoFisher, #22589) for 5 min under UV lamp (XX-15, UVP) under 365 nm wavelength. After washing off remaining Sulfo-Sanpah with sterile PBS, gels were left to air dry for 20 min inside a cell culture hood. PDMS membranes (9 patterns/membrane), passivated in 2% Pluronic F-127 (Sigma, #P2443) in ddH_2O for at least 24 hours, were washed in PBS and air-dried inside a cell culture hood. PDMS membranes were placed on top of the PAA gels, and 50 µl of 0.1 mg/ml of rat tail collagen type I solution (First Link, #112296) was placed on top of the patterns. PAA gels were incubated overnight at 4°C.

Monolayer patterning. PDMS membranes were removed from top of the polyacrylamide gels by first adding sterile PBS. Gels were washed with PBS and incubated with 200 µl of 0.1mg/ml PLL-g-PEG solution (PLL(20)-g[3.5]-PEG(2), SUSOS AG) for 30 min at 37°C. In the meantime, MCF10A cells were trypsinised and counted. Following incubation, gels were washed once with PBS and air-dried for 5 min. 50 µl of MCF10A cell suspension containing 50,000 cells, was placed on top of the gel. Cells were incubated for 1 hour for attachment, the non-attached cells

were washed 3 times with PBS, and cells were incubated in DMEM-F12 media for 24 hr in 5% CO_2 at 37°C.

Drug treatment. After 24 hr incubation, supernatant was aspirated and fresh DMEM-F12 medium containing 4-hydroxytamoxifen (4-OHT, 100 nM, Sigma, #H7904) was added to conditionally express *HRAS*, while equivalent amount of vehicle control, DMSO (1:1000, control) was added to control wells. For proliferation inhibition a CDK1 inhibitor RO-3306 (Sigma Aldrich, #SML0569) was used at 9 μM at the same time as 4-OHT/DMSO treatment and throughout the imaging. To inhibit epithelial tension 10 μM of ROCK inhibitor Y27632 (Sigma Aldrich, #Y0503) or 25 μM myosin II inhibitor **(±)-**Blebbistatin (Sigma Aldrich #203390) was added to media after 6 hours or 24 hours of HRAS-induction (with 4-OHT still present throughout the experiments).

Western Blot. To confirm HRAS induction with 4-OTH, total cell protein lysates were obtained by lysing cells exposed to 100 nM 4-OHT with RIPA buffer (Thermo Fisher, #89900) containing phosphatase inhibitor cocktail 1 and 2 (Sigma Aldrich, P5726 & P2850) and protease inhibitor cocktail (Sigma Aldrich, #11836170001). Protein content was quantified with BCA Protein Assay kit according to manufacturer's instructions (Thermo Fisher, #23227) and 20 μg of protein was mixed with 2x Laemmli buffer (Sigma Aldrich, #S3401) and boiled for 5 min at 95°C. Protein were separated using MOPS buffer (Thermo Fisher, #NP0001) in NuPAGE 4-12% Bis Tris Protein Gels (Thermo Fisher, #NP0323BOX) at 150V for 70 min at RT. Proteins were transferred to a nitrocellulose membrane at 100V for 60 min at 4°C. Membranes were blocked for 30 min in 5% milk in TBST, followed by overnight incubation with primary antibodies diluted in 2.5% milk in TBST. Primary antibodies included rabbit phospho p44/42 MAPK (ERK1/2) (1:2000, Cell Signalling, #4370S), rabbit p44/42 MAPK (Erk1/2) (1:2000, Cell Signalling, #4695S), mouse E-cadherin (1:1000, BD, #610181). Primary antibodies were washed 3 times with TBST, followed by 1 hour incubation with secondary antibodies diluted in 2.5% milk in TBST (1:5000, goat anti-rabbit HRP, or goat anti-mouse HRP, DAKO, #P0448 & #P0447). Membranes were washed 3 times with TBST and exposed to HRP substrate (Immobilon Crescendo, Millipore, #WBLUR0100) for chemiluminescence detection using ChemiDoc™ MP Imaging System (Bio-Rad).

Time-lapse microscopy. Multidimensional acquisitions were performed on an automated inverted microscope (Nikon Ti2 Eclipse, Nikon) using 20x objective (Nikon CFI Plan Apo 20X/0.75 Ph DM). Microscope was equipped with thermal, CO_2 and humidity control, and controlled using NIS software and perfect focus system. Images were obtained every 15 min over 50 hours. Up to 15 independent patterns were imaged in parallel using a motorized XY stage. Patterns were cells formed full monolayers at start of experiments were selected for imaging.

Traction force microscopy. Traction forces were computed from hydrogel displacements through a custom-made software developed in the laboratory of Xavier Trepat, which is based on a Fourier-transform algorithm for elastic hydrogel substrates having finite thickness(*51*). Gel displacements between any experimental time point and a reference image obtained after cell trypsinization were computed by using a custom-made particle imaging velocimetry code developed in the laboratory of Xavier Trepat by using 32-pixel resolution and overlap of 0.5. Patterns for analysis were selected based on quality of beads images – remained in focus throughout the imaging. To define the outer and inner domain, the binary mask of epithelia (identified by filling in their contour) was divided into concentric rings that are one single pixel in thickness. Rings are then labelled through integers 1 to n moving from the edge of the pattern towards its center. The external and internal subdomain are identified by grouping adjacent rings together – the first m rings from the edge (labels 1 to m) are merged together to form the external subdomain whereas the remaining n-m rings are merged together to form the inner subdomain

(the core of the disk). The label *m* is determined in such a way that both domains contain the same amount of pixels/data for unbiased statistical analyses over the two subdomains. The algorithm was implemented in Matlab for automatic execution on the individual mask of epithelia at each time point.

Monolayer stress microscopy. Inter-cellular and intra-cellular stresses in non-transformed MCF10A monolayers were computed via Monolayer Stress Microscopy(*30*) via a custom software implemented via the custom FEM-platform EMBRYO developed in the laboratory of José Muñoz. Briefly, the forces exerted by the elastic hydrogel substrate on the MCF10A epithelium (as a reaction to the traction force field transferred by the epithelium to the substrate) are equilibrated by the tensorial stress state within the epithelium. A necessary condition for the application of this technique is that epithelia maintain their monolayer architecture, a hypothesis only valid for non-transformed MCF10A monolayers in this study.

Immunofluorescence. Cells were fixed with 4% paraformaldehyde (PFA, Santa Cruz, #sc-281692) for 10 min and washed with PBS. Samples were incubated with block buffer containing 1% bovine serum albumin (BSA, Sigma, #A7906) and 0.3% Triton-X100 (Sigma, #T8787) in PBS at RT for 1 hr. Primary antibodies (mouse E-cadherin, 1:1500, BD Biosciences, #610181; mouse integrin β1, 1:250, Abcam, ab30394; rabbit pMLC2, 1:50, Cell Signalling, #3671S) were diluted in block buffer and incubated on top of samples overnight at 4°C. Subsequently, samples were incubated with secondary antibodies (FITC anti-mouse, 1:1000, Jackson Immuno Research, #715-545-150; AlexaFluor564 anti-rabbit, 1:500, Thermo Fisher, #A11035) for 2hr at RT. F-actin was stained by incubating for 30 min with phalloidin-iFluor594 cytoPainter (1:2000, Abcam, #ab176757) or Phalloidin-Atto 647N (1:1000, Sigma-Aldrich, #65906) at RT. In between steps, samples were washed with wash buffer (0.05% Tween-20 (Sigma, #P9416) in PBS). Samples were covered with Fluoroshield mounting medium containing DAPI (Sigma, #F6057) and stored at 4°C until imaging.

Microscopy. Fluorescent images of the patterns were acquired with an inverted microscope (Nikon Ti2 Eclipse, Nikon) with an objective 20x/0.75 (Nikon CFI Plan Apo 20X/0.75 Ph DM). Confocal images were taken using inverted confocal microscope Axio Observer 7 (Spectral Detection Zeiss LSM 800) using 40x/1.3 Oil DIC M27 or 63x/1.4 Oil DIC M27 objectives, with ZEN 2.3 imaging software. For integrin imaging, Zeiss Axiovert 200M microscope was used with 20x and 40x objective. For pMLC2 imaging, Zeiss LSM 780 microscope was used with 20x/0.8 M27 Plan-Apochromat and 40x/1.20 W Korr M27 C-Apochromat objectives using ZEN 2.1 SP3 software.

Nanoindentation. Monolayer stiffness (Young's modulus) was measured by means of the Piuma Nanoindenter (from Optics 11) fitted with a cantilever having stiffness of 0.05 N/m and spherical tip with a radius of 10 μm. Four measurements were taken from 3 different samples. The Young's modulus of tissues before oncogene induction resulted to be 1.363±0.504 kPa (Mean±SD).

Image analysis. In order to detect the physical properties of the epithelial monolayer from fluorescent images a pipeline was created in CellProfiler(*52*) and followed by post processing of the images and data in custom-made automatic workflow in MATLAB (License Number 284992). Images of nuclei and F-actin were used to detect both the individual nuclei and cell borders within monolayers. The intensity of the images was rescaled to the full range of the intensity histograms (minimum 0, maximum 1) and uneven illumination was corrected by subtracting a spline illumination function. Nuclei were segmented using the adaptive Otsu three-class thresholding with the middle intensity class assigned as the background. To improve detection, we optimized minimum diameter (16-pixel unit) and threshold correction factor (0.8). Clumped objects were distinguished by intensity and cell outlines by propagation method. The

precision of nuclei detection was assessed by comparing the outcomes of the pipeline with manual nuclei detection in ImageJ. Features extracted from the image processing included cell ID, nuclei centers coordinates, areas and perimeters. Using custom-made workflow in MATLAB (License Number 284992), we calculated cell and nuclei shape indices and removed outliers (based on surface areas, shape index, nucleus areas).

E-cadherin analysis. To measure E-cadherin intensity a line was drawn using Fiji ImageJ(*53*) (version 1.53c) between two nuclei. The intensity range was then normalized by subtracting the 1st percentile and dividing by 99th percentile. The junctional intensity was extracted, and the ratio between junctional and cytoplasmic intensity was calculated by dividing the junctional value by average of the cytoplasmic value. **Integrin analysis.** To measure integrin intensity a global intensity value of the total image was obtained with ImageJ. **pMLC2 analysis.** Fluorescence intensity was determined using Fiji. Rectangular shape (531.37x290 μm) was placed from one end of the image to other encompassing the middle part of the pattern and the average intensity was measured. The background intensity was removed by calculating intensity in area outside of the pattern for each image. Data from three independent patterns were presented as mean ±standard error.

Data analysis. To perform statistical analysis GraphPad Prism (version 9.0.0) was used. Data distribution was assessed using D'Agostino and Pearson omnibus normality test. Data from all conditions had to pass the normality test to be included in parametric testing. For non-parametric data: a) two groups – Mann Whitney test; b) more than two groups – Kruskal-Wallis statistic test used with Dunn's Multiple Comparison Test; c) two groups over long time-course – 2-way ANOVA with Bonferroni post-test; d) one condition over long time-course – Friedman test with Dunn's multiple comparison test. P-value below 0.5 indicated statistical significance (*p<0.05, **p<0.01, ***p<0.001).

Computational model. The evolution of the net radial-traction components is modelled by resorting to a two-dimensional Finite Element (FE) model of the flat tissue. The flat tissue is represented by a circular domain Ω with radius *R*, with two distinct subdomains: subdomain Ω_1 subjected to a constant baseline contractile force ε_0^c (pre-strain) and subdomain Ω_2 subjected to an additional active contractile strain ε^c, for a total contractile strain of $\varepsilon = \varepsilon_0^c + \varepsilon^c$ (Fig.4B). The radius of the central subdomain Ω_1 decreases in time from *R* (pre-transformation levels) to $r = {}^{R}/_{3}$ to emulate the shape of the pMLC2 trend (Fig. 5 C). The underlaying substrate is modelled as a set of nodal locations fixed in time. The elastic domains Ω_1 and Ω_2 develop local tension because of these prescribed strains. Moreover, each domain is subjected to a specific degree of a solid viscoelastic adhesion with the underlying substrate (*44*), which is specifically modelled via a Kelvin-Voight model of elastic constant. Weakening of cell-matrix adhesion is simulated by applying a reduction factor α to the cell-matrix adhesion constant κ. The subdomains Ω_1 and Ω_2 are assumed to have linear elastic behavior and tissue motion is determined in the approximation of quasi-static equilibrium – there, the active contractility ε^c and the baseline pre-strain ε_0^c equilibrate the passive elastic forces within the tissue and the adhesion forces with the substrate. Model's deformations in each subdomain Ω_1 and Ω_2 were determined via Cauchy's equation

$$\nabla \cdot \boldsymbol{\sigma} + \boldsymbol{f} = \mathbf{0}, \qquad (1)$$

where:

$\boldsymbol{\sigma}$ is the elastic stress tensor given by $\boldsymbol{\sigma} = \lambda\, trace(\boldsymbol{\varepsilon}^e) + 2\mu\boldsymbol{\varepsilon}^e$;

$\boldsymbol{\varepsilon}^e$ is the elastic strain, with $\boldsymbol{\varepsilon}^e = \boldsymbol{\varepsilon} - \varepsilon_0^c\boldsymbol{I}$ in Ω_1 and $\boldsymbol{\varepsilon}^e = \boldsymbol{\varepsilon} - (\varepsilon_0^c + \varepsilon^c)\boldsymbol{I}$ in Ω_2;

$\lambda = E\nu/((1+\nu)(1-2\nu))$. and $\mu = E/(2(1+\nu))$ are the Lamé elasticity constants;

E is the Young modulus and ν the Poisson ratio of both subdomains Ω_1 and Ω_2;

$\boldsymbol{f} = \alpha k\boldsymbol{u}$ is the adhesion force between the tissue and the substrate;

$\boldsymbol{u}$ is the tissue displacement and u_i its components;
$\varepsilon_{ij} = 0.5(\partial_i u_j + \partial_j u_i)$ is the total (observable) strain; and,
α is the weakening factor of the tissue adhesion forces with the substrate.
We use the Finite Element Method to turn equation (1) into a linear system of equations

$$(\mathbf{K} + \mathbf{K}_s)\mathbf{u} = \mathbf{f} \qquad (2)$$

where $\mathbf{K}$ and $\mathbf{K}_s$ are the stiffness matrices corresponding to the elastic and adhesive contributions respectively.
The force vector $\mathbf{f}$ in equation (2) represents the resulting contractile force due to active contractile strain ε^c and/or baseline pre-strain ε_0^c. The time evolution of α, ε^c and ε_0^c.are given in Supplemental Table S1. Vector $\mathbf{f}$ includes the assembling of vectoral contributions $\mathbf{f_1}$ and $\mathbf{f_2}$ respectively from the subdomains Ω_1 and Ω_2, with:
$\mathbf{f_1} = \varepsilon_0^c \int_{\Omega_1} \mathbf{B}^T \mathbf{D}\{1\ 1\ 0\}^T\, d\Omega$ and $\mathbf{f_2} = (\varepsilon_0^c + \varepsilon^c) \int_{\Omega_2} \mathbf{B}^T \mathbf{D}\{1\ 1\ 0\}^T\, d\Omega$
where:
$\mathbf{B}$ is the deformation matrix such that $\boldsymbol{\varepsilon} = \mathbf{Bu}$;
$\mathbf{D}$ is the elasticity matrix that depends on E and ν.
Finally, the discretization of the FE mesh employed 7860 square elements (100 elements along the diameter). We then used experimental data to set: i) the bulk stiffness of the epithelium as having a value of 1kPa prior to *HRAS* activation – this is based on nanoindentation measurements of MCF10A epithelia having an *in vitro* stiffness of 1.36kPa ±0.5kPa (see Materials & Methods). Furthermore, for the sake of simplicity, we also set: ii) the Poisson-Ration of the tissue elasticity to ν=0.46 (quasi-incompressibility); iii) the drop in adhesion with the substrate to a monotonic decrease (Fig. 6 B,E) emulating the average drop in the expression of the collagen receptor integrin β1 within 24 hours from *RAS* activation (Fig. 4 E-F); and, iv) a linear increase in local contractile strain $\varepsilon = \varepsilon_0^c + \varepsilon^c$ (Fig. 6 B,F) to a value approximately double that of the homeostatic baseline – this is based on combined pMLC2 fluorescence intensity from bottom and top layers of the *RAS*-transformed bilayer (Fig. 5 F,H) that approximately amounts to double that of non-transformed monolayers (Fig. 5 C). All model's parameters are summarized in Table S1 of the Supplementary Materials.

References

1. R. Farhadifar, J. C. Röper, B. Aigouy, S. Eaton, F. Jülicher, The Influence of Cell Mechanics, Cell-Cell Interactions, and Proliferation on Epithelial Packing. *Current Biology*. **17**, 2095–2104 (2007).
2. L. Kocgozlu, T. B. Saw, A. P. Le, I. Yow, M. Shagirov, E. Wong, R.-M. Mège, C. T. Lim, Y. Toyama, B. Ladoux, Epithelial Cell Packing Induces Distinct Modes of Cell Extrusions. *Current Biology*. **26**, 2942–2950 (2016).
3. S. Ohsawa, J. Vaughen, T. Igaki, Cell Extrusion: A Stress-Responsive Force for Good or Evil in Epithelial Homeostasis. *Dev Cell*. **44**, 284–296 (2018).
4. J. Fadul, J. Rosenblatt, The forces and fates of extruding cells. *Current Opinion in Cell Biology*. **54**, 66–71 (2018).
5. C. Guillot, T. Lecuit, Mechanics of Epithelial Tissue Homeostasis and Morphogenesis. *Science*. **340**, 1185–1189 (2013).
6. K. L. Mui, C. S. Chen, R. K. Assoian, The mechanical regulation of integrin–cadherin crosstalk organizes cells, signaling and forces. *J Cell Sci*. **129**, 1093–1100 (2016).
7. T. G. Bivona, Dampening oncogenic RAS signaling. *Science*. **363**, 1280–1281 (2019).
8. S. Li, A. Balmain, C. M. Counter, A model for RAS mutation patterns in cancers: finding the sweet spot. *Nature Reviews Cancer*. **18**, 767–777 (2018).
9. C. Gullekson, G. Cojoc, M. Schürmann, J. Guck, A. Pelling, Mechanical mismatch between Ras transformed and untransformed epithelial cells. *Soft Matter*. **13**, 8483–8491 (2017).
10. C. Schäfer, A. Mohan, W. Burford, M. K. Driscoll, A. T. Ludlow, W. E. Wright, J. W. Shay, G. Danuser, Differential Kras V12 protein levels control a switch regulating lung cancer cell morphology and motility. *Converg. Sci. Phys. Oncol.* **2**, 035004 (2016).

11. D. H. Nguyen, A. D. Catling, D. J. Webb, M. Sankovic, L. A. Walker, A. V. Somlyo, M. J. Weber, S. L. Gonias, Myosin light chain kinase functions downstream of Ras/ERK to promote migration of urokinase-type plasminogen activator-stimulated cells in an integrin-selective manner. *J Cell Biol*. **146**, 149–164 (1999).
12. J. C. Chen, S. Zhuang, T. H. Nguyen, G. R. Boss, R. B. Pilz, Oncogenic Ras Leads to Rho Activation by Activating the Mitogen-activated Protein Kinase Pathway and Decreasing Rho-GTPase-activating Protein Activity *. *Journal of Biological Chemistry*. **278**, 2807–2818 (2003).
13. K. Magudia, A. Lahoz, A. Hall, K-Ras and B-Raf oncogenes inhibit colon epithelial polarity establishment through up-regulation of c-myc. *J Cell Biol*. **198**, 185–194 (2012).
14. C.-A. Schoenenberger, K. S. Matlin, Cell polarity and epithelial oncogenesis. *Trends in Cell Biology*. **1**, 87–92 (1991).
15. C. Hogan, S. Dupré-Crochet, M. Norman, M. Kajita, C. Zimmermann, A. E. Pelling, E. Piddini, L. A. Baena-López, J.-P. Vincent, Y. Itoh, H. Hosoya, F. Pichaud, Y. Fujita, Characterization of the interface between normal and transformed epithelial cells. *Nature Cell Biology*. **11**, 460–467 (2009).
16. M. Kajita, K. Sugimura, A. Ohoka, J. Burden, H. Suganuma, M. Ikegawa, T. Shimada, T. Kitamura, M. Shindoh, S. Ishikawa, S. Yamamoto, S. Saitoh, Y. Yako, R. Takahashi, T. Okajima, J. Kikuta, Y. Maijima, M. Ishii, M. Tada, Y. Fujita, Filamin acts as a key regulator in epithelial defence against transformed cells. *Nature Communications*. **5**, 4428 (2014).
17. S. Chagnon-Lessard, H. Jean-Ruel, M. Godin, A. E. Pelling, Mechanotransduction of strain regulates an invasive phenotype in newly transformed epithelial cells. *bioRxiv*. **1**, 1–14 (2019).
18. S. K. Wu, A. K. Lagendijk, B. M. Hogan, G. A. Gomez, A. S. Yap, Active contractility at E-cadherin junctions and its implications for cell extrusion in cancer. *Cell cycle (Georgetown, Tex.)*. **14**, 315–322 (2015).
19. C. Bielmeier, S. Alt, V. Weichselberger, M. La Fortezza, H. Harz, F. Jülicher, G. Salbreux, A.-K. Classen, Interface Contractility between Differently Fated Cells Drives Cell Elimination and Cyst Formation. *Current Biology*. **26**, 563–574 (2016).
20. J. L. Teo, G. A. Gomez, S. Weeratunga, E. M. Davies, I. Noordstra, S. Budnar, H. Katsuno-Kambe, M. J. McGrath, S. Verma, V. Tomatis, B. R. Acharya, L. Balasubramaniam, R. M. Templin, K.-A. McMahon, Y. S. Lee, R. J. Ju, S. J. Stebhens, B. Ladoux, C. A. Mitchell, B. M. Collins, R. G. Parton, A. S. Yap, Caveolae Control Contractile Tension for Epithelia to Eliminate Tumor Cells. *Developmental Cell*. **54**, 75-91.e7 (2020).
21. W. Hill, A. Zaragkoulias, B. Salvador-Barbero, G. J. Parfitt, M. Alatsatianos, A. Padilha, S. Porazinski, T. E. Woolley, J. P. Morton, O. J. Sansom, C. Hogan, EPHA2-dependent outcompetition of KRASG12D mutant cells by wild-type neighbors in the adult pancreas. *Current Biology* (2021), doi:10.1016/j.cub.2021.03.094.
22. S. K. Wu, A. K. Lagendijk, B. M. Hogan, G. A. Gomez, A. S. Yap, Active contractility at E-cadherin junctions and its implications for cell extrusion in cancer. *Cell Cycle*. **14**, 315–322 (2015).
23. S. Chagnon-Lessard, H. Jean-Ruel, M. Godin, A. E. Pelling, Mechanotransduction of Strain Regulates an Invasive Phenotype in Newly Transformed Epithelial Cells. *Front. Phys*. **9** (2021), doi:10.3389/fphy.2021.654613.
24. S. Porazinski, J. de Navascués, Y. Yako, W. Hill, M. R. Jones, R. Maddison, Y. Fujita, C. Hogan, EphA2 Drives the Segregation of Ras-Transformed Epithelial Cells from Normal Neighbors. *Current Biology*. **26**, 3220–3229 (2016).
25. D. A. Prober, B. A. Edgar, Interactions between Ras1, dMyc, and dPI3K signaling in the developing Drosophila wing. *Genes Dev*. **16**, 2286–2299 (2002).
26. H. A. Messal, S. Alt, R. M. M. Ferreira, C. Gribben, V. M.-Y. Wang, C. G. Cotoi, G. Salbreux, A. Behrens, Tissue curvature and apicobasal mechanical tension imbalance instruct cancer morphogenesis. *Nature*. **566**, 126–130 (2019).
27. M. Molina-Arcas, D. C. Hancock, C. Sheridan, M. S. Kumar, J. Downward, Coordinate direct input of both KRAS and IGF1 receptor to activation of PI 3-kinase in KRAS mutant lung cancer. *Cancer Discov*. **3**, 548–563 (2013).
28. M. Plodinec, M. Loparic, C. A. Monnier, E. C. Obermann, R. Zanetti-Dallenbach, P. Oertle, J. T. Hyotyla, U. Aebi, M. Bentires-Alj, R. Y. H. Lim, C.-A. Schoenenberger, The nanomechanical signature of breast cancer. *Nature Nanotechnology*. **7**, 757–765 (2012).
29. R. Reuten, S. Zendehroud, M. Nicolau, L. Fleischhauer, A. Laitala, S. Kiderlen, D. Nikodemus, L. Wullkopf, S. R. Nielsen, S. McNeilly, C. Prein, M. Rafaeva, E. M. Schoof, B. Furtwängler, B. T. Porse, H. Kim, K. J. Won, S. Sudhop, K. W. Zornhagen, F. Suhr, E. Maniati, O. M. T. Pearce, M. Koch, L. B. Oddershede, T. Van Agtmael, C. D. Madsen, A. E. Mayorca-Guiliani, W. Bloch, R. R. Netz, H. Clausen-

Schaumann, J. T. Erler, Basement membrane stiffness determines metastases formation. *Nature Materials*, 1–12 (2021).
30. X. Serra-Picamal, V. Conte, R. Sunyer, J. J. Muñoz, X. Trepat, in *Methods in Cell Biology*, E. K. Paluch, Ed. (Academic Press, 2015; http://www.sciencedirect.com/science/article/pii/S0091679X14000375), vol. 125 of *Biophysical Methods in Cell Biology*, pp. 309–330.
31. A. F. Mertz, S. Banerjee, Y. Che, G. K. German, Y. Xu, C. Hyland, M. C. Marchetti, V. Horsley, E. R. Dufresne, Scaling of traction forces with the size of cohesive cell colonies. *Physical Review Letters*. **108** (2012), doi:10.1103/PhysRevLett.108.198101.
32. S. Banerjee, M. C. Marchetti, Contractile stresses in cohesive cell layers on finite-thickness substrates. *Physical Review Letters*. **109** (2012), doi:10.1103/PhysRevLett.109.108101.
33. Y. Zhang, X. Shi, T. Zhao, C. Huang, Q. Wei, X. Tang, L. C. Santy, M. T. A. Saif, S. Zhang, A traction force threshold signifies metastatic phenotypic change in multicellular epithelia. *Soft Matter*. **15**, 7203–7210 (2019).
34. J. Notbohm, S. Banerjee, K. J. C. Utuje, B. Gweon, H. Jang, Y. Park, J. Shin, J. P. Butler, J. J. Fredberg, M. C. Marchetti, Cellular Contraction and Polarization Drive Collective Cellular Motion. *Biophysical Journal*. **110**, 2729–2738 (2016).
35. M. Deforet, V. Hakim, H. G. Yevick, G. Duclos, P. Silberzan, Emergence of collective modes and tri-dimensional structures from epithelial confinement. *Nature Communications*. **5**, 1–9 (2014).
36. C. Pérez-González, R. Alert, C. Blanch-Mercader, M. Gómez-González, T. Kolodziej, E. Bazellieres, J. Casademunt, X. Trepat, Active wetting of epithelial tissues. *Nature Physics*. **15** (2019), doi:10.1038/s41567-018-0279-5.
37. S. Neelam, P. R. Hayes, Q. Zhang, R. B. Dickinson, T. P. Lele, Vertical uniformity of cells and nuclei in epithelial monolayers. *Scientific Reports*. **6**, 19689 (2016).
38. Q. Li, R. R. Mattingly, Restoration of E-cadherin Cell-Cell Junctions Requires Both Expression of E-cadherin and Suppression of ERK MAP Kinase Activation in Ras-Transformed Breast Epithelial Cells. *Neoplasia*. **10**, 1444–1458 (2008).
39. C. R. Schmidt, Y. J. Gi, R. J. Coffey, R. D. Beauchamp, A. S. Pearson, Oncogenic Ras dominates overexpression of E-cadherin in malignant transformation of intestinal epithelial cells. *Surgery*. **136**, 303–309 (2004).
40. C. R. Schmidt, M. K. Washington, Y. J. Gi, R. J. Coffey, R. D. Beauchamp, A. S. Pearson, Dysregulation of E-cadherin by oncogenic ras in intestinal epithelial cells is blocked by inhibiting MAP kinase. *The American Journal of Surgery*. **186**, 426–430 (2003).
41. N. C. Heer, A. C. Martin, Tension, contraction and tissue morphogenesis. *Development*. **144**, 4249–4260 (2017).
42. P. Chugh, A. G. Clark, M. B. Smith, D. A. D. Cassani, K. Dierkes, A. Ragab, P. P. Roux, G. Charras, G. Salbreux, E. K. Paluch, Actin cortex architecture regulates cell surface tension. *Nature Cell Biology*. **19**, 689–697 (2017).
43. Z. M. Goeckeler, R. B. Wysolmerski, Myosin light chain kinase-regulated endothelial cell contraction: the relationship between isometric tension, actin polymerization, and myosin phosphorylation. *Journal of Cell Biology*. **130**, 613–627 (1995).
44. A. Christensen, A.-K. V. West, L. Wullkopf, J. T. Erler, L. B. Oddershede, J. Mathiesen, Friction-limited cell motility in confluent monolayer tissue. *Phys. Biol.* **15**, 066004 (2018).
45. K. A. Rauen, The RASopathies. *Annu. Rev. Genom. Hum. Genet.* **14**, 355–369 (2013).
46. H. K. Matthews, S. Ganguli, K. Plak, A. V. Taubenberger, Z. Win, M. Williamson, M. Piel, J. Guck, B. Baum, Oncogenic Signaling Alters Cell Shape and Mechanics to Facilitate Cell Division under Confinement. *Developmental Cell*. **52**, 563-573.e3 (2020).
47. J. Ling, M. Sckaff, M. Tiwari, Y. Chen, J. Li, J. Jones, G. L. Sen, RAS-mediated suppression of PAR3 and its effects on SCC initiation and tissue architecture occur independently of hyperplasia. *Journal of Cell Science*. **133** (2020), doi:10.1242/jcs.249102.
48. S. Porazinski, J. de Navascués, Y. Yako, W. Hill, M. R. Jones, R. Maddison, Y. Fujita, C. Hogan, EphA2 Drives the Segregation of Ras-Transformed Epithelial Cells from Normal Neighbors. *Current Biology*. **26**, 3220–3229 (2016).
49. J. Ling, M. Sckaff, M. Tiwari, Y. Chen, J. Li, J. Jones, G. L. Sen, RAS-mediated suppression of PAR3 and its effects on SCC initiation and tissue architecture occur independently of hyperplasia. *J Cell Sci*. **133** (2020), doi:10.1242/jcs.249102.
50. J. Debnath, S. K. Muthuswamy, J. S. Brugge, Morphogenesis and oncogenesis of MCF-10A mammary epithelial acini grown in three-dimensional basement membrane cultures. *Methods*. **30**, 256–268 (2003).

51. X. Trepat, M. R. Wasserman, T. E. Angelini, E. Millet, D. A. Weitz, J. P. Butler, J. J. Fredberg, Physical forces during collective cell migration. *Nature Physics* (2009), doi:10.1038/nphys1269.
52. A. E. Carpenter, T. R. Jones, M. R. Lamprecht, C. Clarke, I. H. Kang, O. Friman, D. A. Guertin, J. H. Chang, R. A. Lindquist, J. Moffat, P. Golland, D. M. Sabatini, CellProfiler: Image analysis software for identifying and quantifying cell phenotypes. *Genome Biology* (2006), doi:10.1186/gb-2006-7-10-r100.
53. J. Schindelin, I. Arganda-Carreras, E. Frise, V. Kaynig, M. Longair, T. Pietzsch, S. Preibisch, C. Rueden, S. Saalfeld, B. Schmid, J.-Y. Tinevez, D. J. White, V. Hartenstein, K. Eliceiri, P. Tomancak, A. Cardona, Fiji - an Open Source platform for biological image analysis. *Nat Methods*. **9** (2012), doi:10.1038/nmeth.2019.

Acknowledgements

This work was supported by the Spanish Ministry MICINN /FEDER (grants BFU2016-75101-P and RYC-2014-15559 to V.C., DPI2016-74929-R to J.J.M., BES-2017-081337 to G.F., BES-2013-062633 to M.U.); the Generalitat de Catalunya (grant 2017SGR1278 to J.J.M.); the IBEC-ICMS Exchange Program fund to A.N. for nanoindentation measurements; H.K.M was supported by a CRUK/EPSRC Multi-disciplinary Project Award (C1529/A23335) and the MRC/UCL Laboratory for Molecular Cell Biology (MC_CF12266). The Spanish Ministry (MICINN) and its funding programs (Severo Ochoa, FPI, Excelencia) along with the CERCA Program of the Generalitat de Catalunya support research at the IBEC. The authors would also like to thank: Carlos Pérez-González (IBEC); Víctor González-Tarragó (IBEC); Manuel Gómez González (IBEC); Zanetta (Jenny) Kechagia (IBEC); Prof Bouten (TU/e, ICMS); and, Janine Grolleman (TU/e, ICMS) for helpful technical advice and support.

Author contributions

A.N. and V.C. designed experiments; A.N. performed all experiments with contributions from S.D., G.F. and H.M.; A.N., M.U. and H.M. designed protocols; J.M. designed and implemented the computational model; B.B. and H.M. provided the cellular model; X.T. provided custom software for Traction Force Microscopy; A.N., J.M., S.D. and V.C. performed data analysis; A.N., J.M., S.D., X.T., H.M., B.B. and V.C. interpreted data; V.C. conceived the study, secured the funding and supervised the project. A.N., J.M., H.M. and V.C. wrote the manuscript, which all authors reviewed and edited.

Competing interests

The authors declare no competing interests.

Data availability

All data supporting the findings of this study are available from the corresponding author upon reasonable request.

Code availability

Custom code may be made available from the corresponding author upon reasonable request.

Figure Legends

Fig. 1. Morphological characterization of normal and *HRAS*-transformed MCF10A tissues. (**A**) Schematic of the experimental setup. (**B**) *HRAS* induction confirmed by increase in phosphorylation of MAPK (ERK1/2) shown in representative Western Blots. (**C**) Phase contrast time-lapse of selected non-transformed (control) and *HRAS*-transformed MCF10A monolayers (imaging starts at t=-4 hours and *HRAS*-activation is induced at t=0 hours; scale bar is 200 μm). (**D**) Contours of epithelia shown in panel C (time progresses with blue, red, green and yellow colors). (**E**) Time-evolution of the surface area of the epithelia's footprint on the substate matrix (epithelial domain); (**F**) time-evolution of the major and minor diameters of the epithelia domain in the case of non-transformed and HRAS-transformed epithelia; (**G**) time-evolution of the epithelial domain's aspect ratio – this quantity is defined as the major axis divided by the minor axis of the epithelial domain's; (**H**) time-evolution of the epithelial domain's circularity; (**I**) cell number in HRAS-transformed epithelia at 12 hr post induction (start of area decline, E) compared to non-transformed epithelia at 12, 24, 44 hr. Kruskal-Wallis test + Dunn's multiple comparisons test. (**E-I**) Statistics over 15 non-transformed epithelia and 16 HRAS-transformed epithelia from at least 4 independent experiment repeats. Each epithelium was imaged for at least 50 hours. (**J**) Time-evolution of the surface area of the non-transformed (n=7) and HRAS-transformed (n=8) epithelia domains during cell cycle arrest (9 μM RO-3306). (E-H, J) Time-evolution graphs represent Mean±S.E.M. of medians at each time point. 2-way ANOVA with Bonferroni post-test, *$p<0.05$

Fig. 2. Mechanical characterization of normal and *HRAS*-transformed MCF10A tissues. Overlays of traction-force vectors (**A-B**) and traction-force magnitude maps (**C-D**) on phase contrast images of confined MCF10A epithelia; (**A,C**) representative non-transformed epithelium at t=19 hours; (**B,D**) representative *HRAS*-transformed epithelium at t=45 hours. (**E**) Schematic representing the whole epithelial domain along with its outer and inner subdomains. (**F-K**) Time evolution of magnitudes and components of the traction-force field in the whole epithelial domain (blue) as well as in the inner (orange) and outer (green) epithelial subdomains. (**F-G**) Time evolution of the average Traction-field ±magnitude for (**F**) non-transformed epithelia and (**G**) *HRAS*-transformed epithelia. (**H-K**) Time evolution of the average traction force components: (**H-I**) perpendicular to the epithelial domain's edge ($T_\perp$) for (**H**) non-transformed and (**I**) *HRAS*-transformed epithelia; (**J-K**) tangential to the epithelial domain's edge ($T_\parallel$) for (**J**) non-transformed and (**K**) *HRAS*-transformed epithelia. (**L-M**) Kymographs of the radial (perpendicular) component of the traction field $T_\perp$: (**L**) for a representative non-transformed MCF10A epithelium and (**M**) for a representative *HRAS*-transformed MCF10A epithelium. White lines represent the average evolution of the edge of the island in time, the center of the island colocalizing with the bottom of the graph. A negative component $T_\perp$ (red) means that the corresponding traction-force vector is in oriented towards the exterior of the epithelial domain's edge, whereas a positive component $T_\perp$ (green) is indicative of traction-force orientation toward the interior of the epithelial domain's edge. (**F-K**) Statistics over 15 non-transformed epithelia and 16 *HRAS*-transformed epithelia from at least 4 independent experiment repeats. Each epithelium was imaged for at least 50 hours. Median over each epithelial domain at each time point of its evolution. Time-evolution graphs represent Mean±S.E.M of medians at each time point. 2-way ANOVA with Bonferroni post-test, *$p<0.05$.

Figure 3. **Oncogenic *HRAS*-expression induces the bilayering of MCF10A monolayers.** (**A-C**) Measurements of epithelial monolayers features at selected time points for both non-transformed and *HRAS*-transformed epithelia: (**A**) tissue height, (**B**) nucleus height and (**C**) cell area (μm^2). Kruskal-Wallis statistic test with Dunn's Multiple Comparison Test. (**D**) Representative confocal images of non-transformed monolayer (top subpanel) and *HRAS*-transformed bilayer (bottom subpanel) at t=24 hours from oncogene induction – focal planes is

orthogonal to the substrate matrix (z-axis). Actin is labelled in grey and DAPI in blue. Scale bar = 15 μm. (**E**) Representative confocal image of non-transformed monolayer and *HRAS*-transformed bilayer – focal plane crosses the tissue parallelly to the substrate matrix. Actin is labelled in shades of grey and DAPI in blue. Scale bar = 15 μm. (**F-H**) Quantification of cell features in the top and bottom layers of *HRAS*-transformed bilayers: (**F**) cell surface area, (**G**) cell surface perimeter and (**H**) cell shape index. Mean±S.E.M. of median values from at least 3 individual patterns. Mann Whitney test, *** $p<0.001$.

Figure 4. Oncogenic HRAS-expression alters the expression of E-cadherin and β1-integrin. (**A**) Western Blot showing E-cadherin expression in non-transformed (control) and *HRAS*-transformed MCF10A cells over 48 hours from oncogene induction. (**B**) Representative confocal images showing the distribution of E-cadherin at t=0 hours and within non-transformed and *HRAS*-transformed tissues at t=24 hours. E-cadherin labelled in grey, DAPI in blue. Scale bar = 50 μm. (**C-D**) Global E-cadherin fluorescence in non-transformed (control) and *HRAS*-transformed epithelia: (**C**) junctional intensity (normalized) and (**D**) Ratio of junctional to cytoplasmic intensity. (**E**) Confocal images of non-transformed and *HRAS*-transformed epithelia after 7 and 24 hours of oncogene induction stained for E-cadherin (red), DAPI (blue) and integrin β1 (green in panels at the center and shades of greys in panels on the right). Scale bar = 20 μm (**F**) Confocal images of entire non-transformed monolayer and *HRAS*-transformed bilayer after 24 hours of oncogene induction stained for integrin β1 (shades of greys) – focal plane crosses the tissue parallelly to the substrate matrix. Scale bar = 50 μm. (**G**) Intensity of global β1-integrin fluorescence in non-transformed and *HRAS*-transformed epithelia after 7 and 24 hours of oncogene induction. **E-cadherin:** Mean±S.E.M. of median values from at least 3 individual patterns and Kruskal-Wallis statistic test with Dunn's Multiple Comparison Test. **Integrin:** Mean± S.E.M.; 2-way ANOVA with Bonferroni post-test. *$p<0.05$, **$p<0.01$, ***$p<0.001$.

Figure 5. Oncogenic *HRAS*-induction causes a tension differential in the MCF10A bilayers. Representative confocal images of non-transformed monolayer (**A**) and *HRAS*-transformed bilayer **(D)** at t=24 hours from oncogene induction stained for pMLC2, F-actin and DAPI (shades of greys) – focal planes are orthogonal to the substrate matrix. Scale bar = 20 μm. (**B,E,G**) Representative confocal images of entire non-transformed monolayer (**B**) and *HRAS*-transformed bilayer (**E**, bottom layer and **G** top layer of the bilayer) – focal plane crosses the tissue parallelly to the substrate matrix. pMLC2, F-actin and DAPI (nuclei) are labelled either in color code (red, grey and blue respectively) or shades of greys. Scale bar = 50 μm (**C**) Relative fold change in averaged global intensity relative to center of the monolayer of pMLC2 fluorescence from edge to edge of the circular epithelial domain of non-transformed (blue) and *HRAS*-transformed (pink) monolayers (n=3 and mean ± S.D. in blue) (**F)** Relative fold change in averaged global intensity relative to center of the monolayer of F-actin fluorescence from edge to edge of the circular epithelial domain of non-transformed (blue) and transformed (pink) monolayers (n=3 and mean ± S.D. in blue); and (**H**) individual averaged intensity profiles of pMLC2 (red) and F-actin (grey) of a representative section of *HRAS*-transformed top layer.

Figure 6. *In silico* model of *HRAS*-driven mechanical instability in MCF10A circular tissues. (**A-B**) Schematic representing the experimental features captured and emulated by the computational model. (**A**) The epithelium is represented as a 2D continuum (bulk stiffness E and Poisson Ratio ν) having finite thickness in plane-stress approximation (grey). (**B**) Schematic representing the inter- and intra-cellular forces along with the cell-matrix forces at the interface with the elastic substrate. The entire domain of the epithelium is uniformly subjected to a contractile pre-strain constant in time (green arrows, Materials&Methods). A subdomain Ω_2 of the epithelial domain (light grey) can also develop further contractile strain (active tension) – the distribution of tension within the epithelium represented here corresponds to that one illustrated in

subpanel G. Active strain and pre-strain develop contractile tensions that equilibrate passive elastic forces within the epithelium and result in traction forces (magenta arrows) being transferred to the substrate matrix via solid viscoelastic friction (wavy blue elements). (**C**) Finite element discretization of the 2D epithelium with a representative finite element represented in dark grey and outlined in black. (**D**) Decomposition of forces acting at nodes of a representative finite element. (**E**) Schematic illustrating the regions of the epithelial domain where epithelial tension increases (high tension, orange) from pre-transformation levels (baseline tension, green) due to active strain combining with pre-strain. (**F**) Adhesion with the substrate monotonically decreases from pre-transformation levels in correspondence of the entire epithelial domain (i.e. both subdomains Ω_1 and Ω_2). (**G**) Epithelial tension (orange) increases monotonically to double pre-transformation levels in the epithelial subdomain Ω_2 (epithelium's periphery) – this is a consequence of the combined effect of active strain (gray) and pre-strain (green) in Ω_2. (**H-J**) Model's predictions for the trends of epithelial surface area in silico compared to the respective trend in vitro – both trends have been normalized to the first time-point of the imaging time-lapse (i.e. t = - 4 hours). (**K-M**) Model's predictions for the trends of traction force magnitude in silico compared to the respective trend in vitro – both trends have been normalized to the first time-point of the imaging time-lapse (i.e. t = - 4 hours). **(H,K)** Trends in the case of an increase of tension at the epithelium's periphery and a decrease of adhesion throughout the epithelium (subpanels E-G). **(I,L)** Trends in the case of only a decrease of adhesion throughout the epithelium (no increase of tension at the epithelium's periphery). **(J,M)** Trends in the case of only an increase of tension at the epithelium's periphery (no decrease of adhesion throughout the epithelium).

Figure 7. Targeting epithelial tension during HRAS transformation. A) Schematic of the action of inhibitors, **B-E)** Representative phase contrast images of confined non-transformed (Control) and HRAS-transformed MCF10A epithelia treated with ROCK inhibitor Y27632 (10 μM, **B, D**) or myosin II inhibitor Blebbistatin (25 μM, **C, E**) during early transformation (6 hours, **B-C**) or late transformation (24 hours, **D-E**) Scale bar = 100 μm. (**F,H**) Time evolution of normal components of the traction-force field in the outer epithelial subdomains during early (**F**) and late (**H**) transformation in presence of inhibitors. (**G, I**) Time-evolution of the surface area of the epithelia's footprint on the substate matrix during early (**G**) and late (**I**) transformation in presence of inhibitors. Mean±S.E.M of medians at each time point (n=3-5).

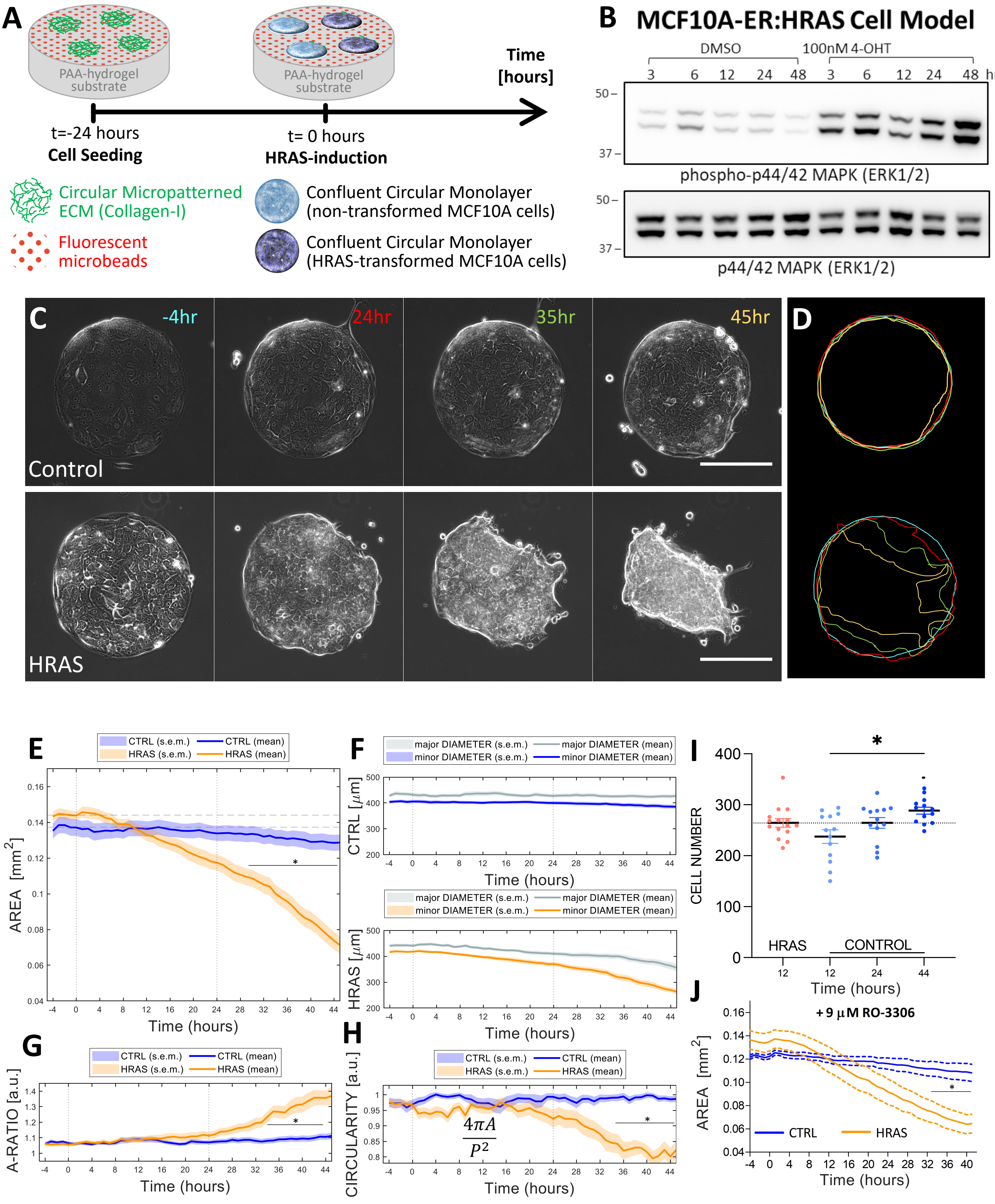
A
PAA-hydrogel substrate
PAA-hydrogel substrate
Time [hours]
t=-24 hours
Cell Seeding
t= 0 hours
HRAS-induction
Circular Micropatterned ECM (Collagen-I)
Fluorescent microbeads
Confluent Circular Monolayer (non-transformed MCF10A cells)
Confluent Circular Monolayer (HRAS-transformed MCF10A cells)
B
MCF10A-ER:HRAS Cell Model
DMSO
100nM 4-OHT
3 6 12 24 48 3 6 12 24 48 hr
50 –
37 –
phospho-p44/42 MAPK (ERK1/2)
p44/42 MAPK (ERK1/2)
C
-4hr
24hr
35hr
45hr
Control
HRAS
D
E
CTRL (s.e.m.)
CTRL (mean)
HRAS (s.e.m.)
HRAS (mean)
AREA [mm²]
Time (hours)
F
major DIAMETER (s.e.m.)
major DIAMETER (mean)
minor DIAMETER (s.e.m.)
minor DIAMETER (mean)
CTRL [μm]
HRAS [μm]
Time (hours)
I
CELL NUMBER
HRAS
CONTROL
Time (hours)
G
A-RATIO [a.u.]
Time (hours)
H
CIRCULARITY [a.u.]
$\frac{4\pi A}{P^2}$
Time (hours)
J
+9 μM RO-3306
AREA [mm²]
CTRL
HRAS
Time (hours)

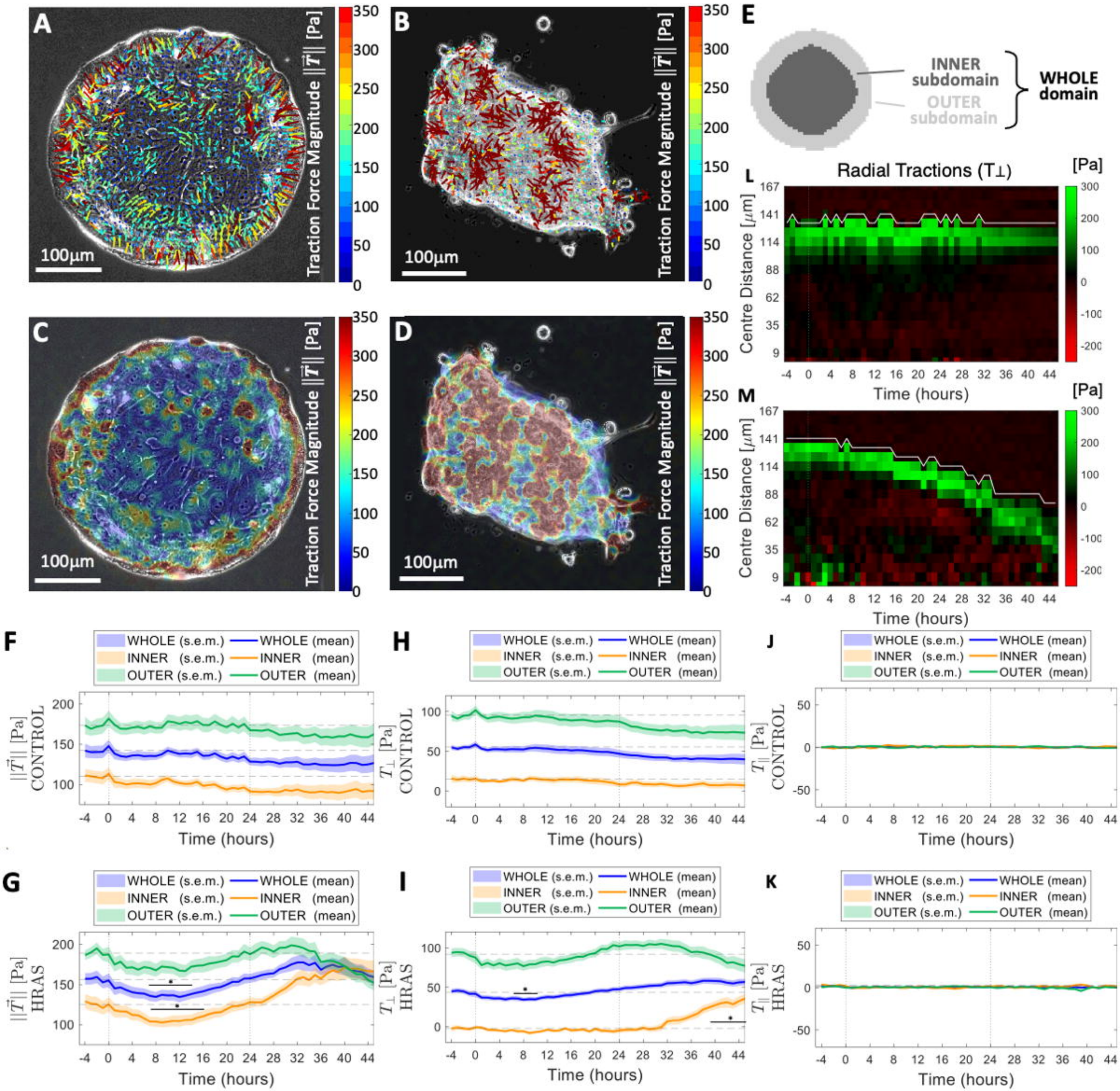
A
B
C
D
E
F
G
H
I
J
K
L
M
100µm
Traction Force Magnitude $\|\vec{T}\|$ [Pa]
INNER subdomain
OUTER subdomain
WHOLE domain
Radial Tractions (T⊥)
[Pa]
Centre Distance [µm]
Time (hours)
WHOLE (s.e.m.)
WHOLE (mean)
INNER (s.e.m.)
INNER (mean)
OUTER (s.e.m.)
OUTER (mean)
$\|\vec{T}\|$ [Pa] CONTROL
$T_\perp$ [Pa] CONTROL
$T_\parallel$ [Pa] CONTROL
$\|\vec{T}\|$ [Pa] HRAS
$T_\perp$ [Pa] HRAS
$T_\parallel$ [Pa] HRAS

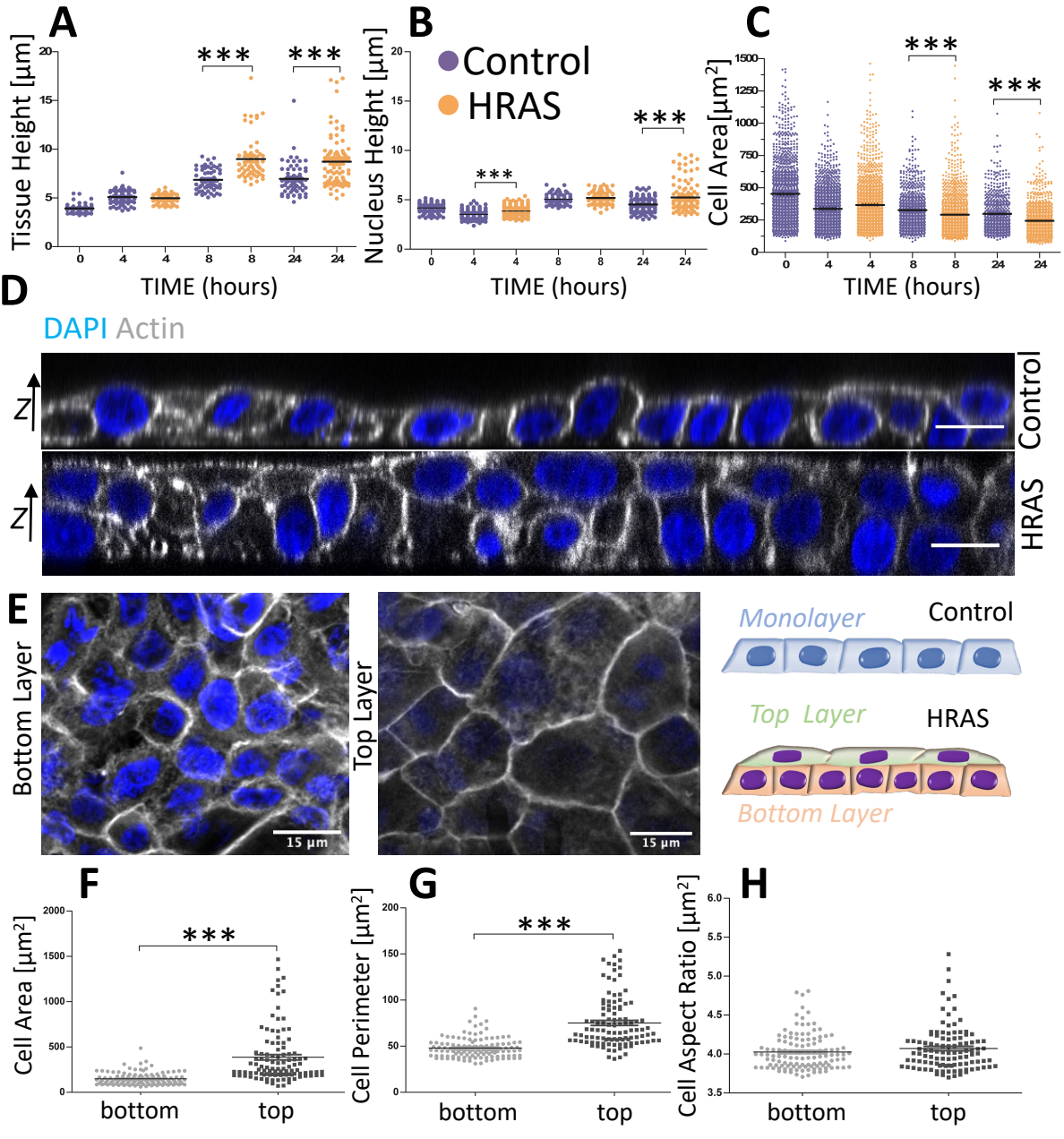
A
Tissue Height [µm]
TIME (hours)
***
***
B
Nucleus Height [µm]
Control
HRAS
TIME (hours)
***
***
C
Cell Area[µm²]
TIME (hours)
***
***
D
DAPI Actin
Z
Control
Z
HRAS
E
Bottom Layer
15 µm
Top Layer
15 µm
Monolayer
Control
Top Layer
HRAS
Bottom Layer
F
Cell Area [µm²]
***
bottom
top
G
Cell Perimeter [µm²]
***
bottom
top
H
Cell Aspect Ratio [µm²]
bottom
top

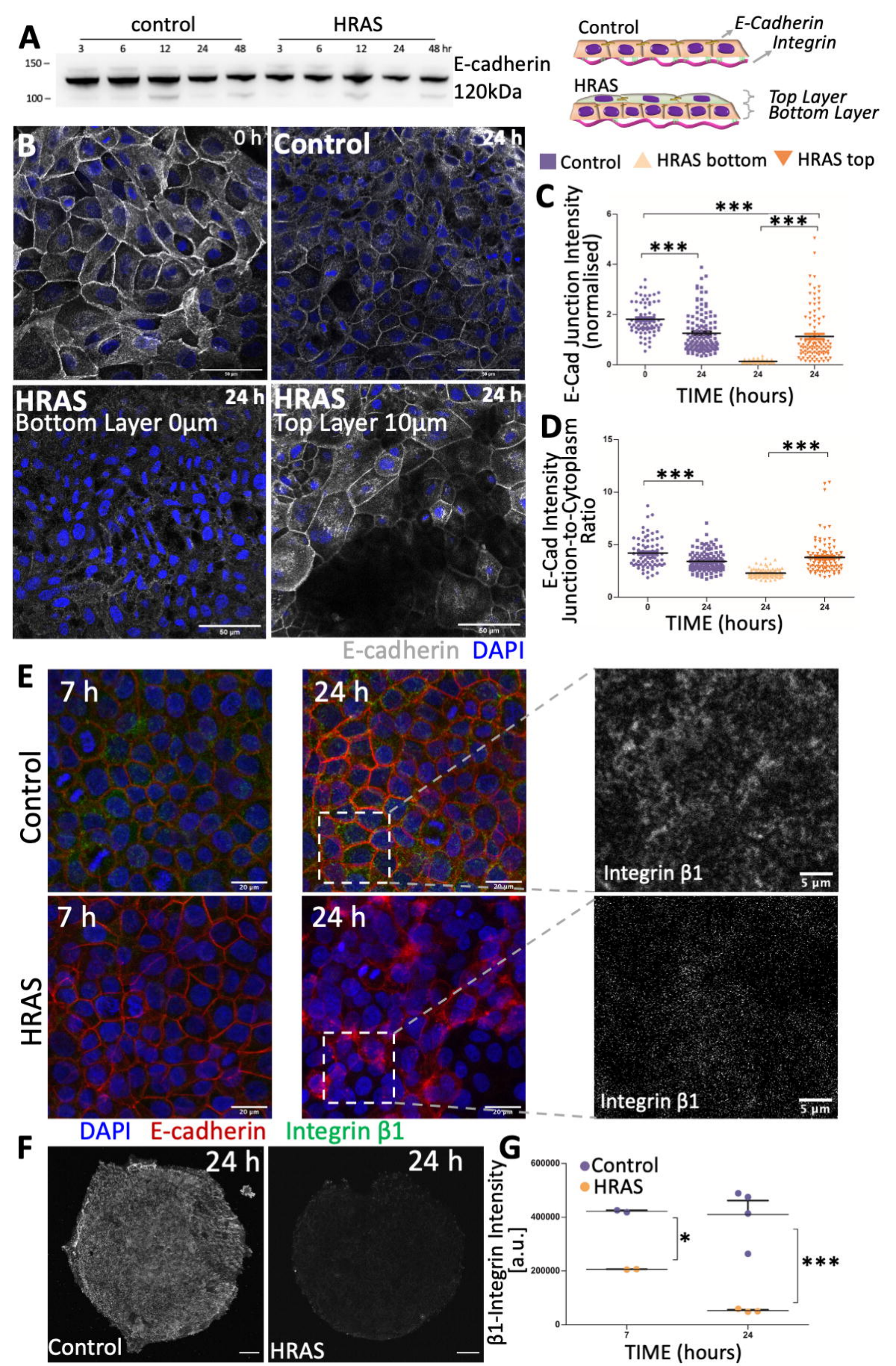
A
control
HRAS
3 6 12 24 48 3 6 12 24 48 hr
150 –
100 –
E-cadherin
120kDa
Control
E-Cadherin
Integrin
HRAS
Top Layer
Bottom Layer
B
0 h
Control
24 h
HRAS
Bottom Layer 0µm
24 h
HRAS
Top Layer 10µm
24 h
50 µm
E-cadherin DAPI
Control
HRAS bottom
HRAS top
C
E-Cad Junction Intensity (normalised)
***
***
***
TIME (hours)
D
E-Cad Intensity Junction-to-Cytoplasm Ratio
***
***
TIME (hours)
E
7 h
24 h
Control
HRAS
Integrin β1
5 µm
20 µm
DAPI E-cadherin Integrin β1
F
24 h
Control
HRAS
G
Control
HRAS
β1-Integrin Intensity [a.u.]
*
***
TIME (hours)

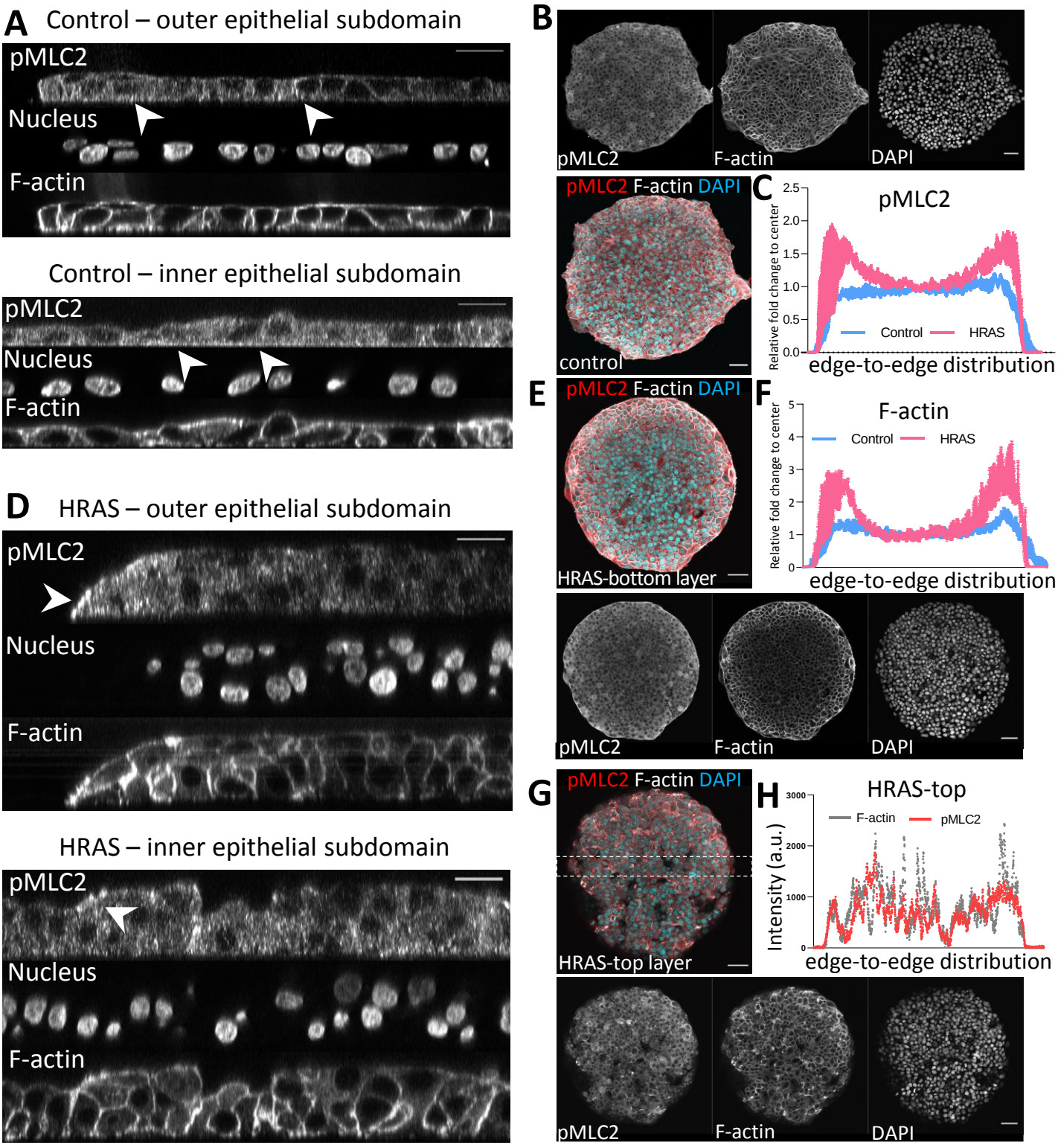
A
Control – outer epithelial subdomain
pMLC2
Nucleus
F-actin
Control – inner epithelial subdomain
pMLC2
Nucleus
F-actin
D
HRAS – outer epithelial subdomain
pMLC2
Nucleus
F-actin
HRAS – inner epithelial subdomain
pMLC2
Nucleus
F-actin
B
pMLC2
F-actin
DAPI
pMLC2 F-actin DAPI
control
C
pMLC2
Relative fold change to center
2.5
2.0
1.5
1.0
0.5
0.0
Control
HRAS
edge-to-edge distribution
E
pMLC2 F-actin DAPI
HRAS-bottom layer
F
F-actin
Control
HRAS
Relative fold change to center
5
4
3
2
1
0
edge-to-edge distribution
pMLC2
F-actin
DAPI
G
pMLC2 F-actin DAPI
HRAS-top layer
H
HRAS-top
F-actin
pMLC2
Intensity (a.u.)
3000
2000
1000
0
edge-to-edge distribution
pMLC2
F-actin
DAPI

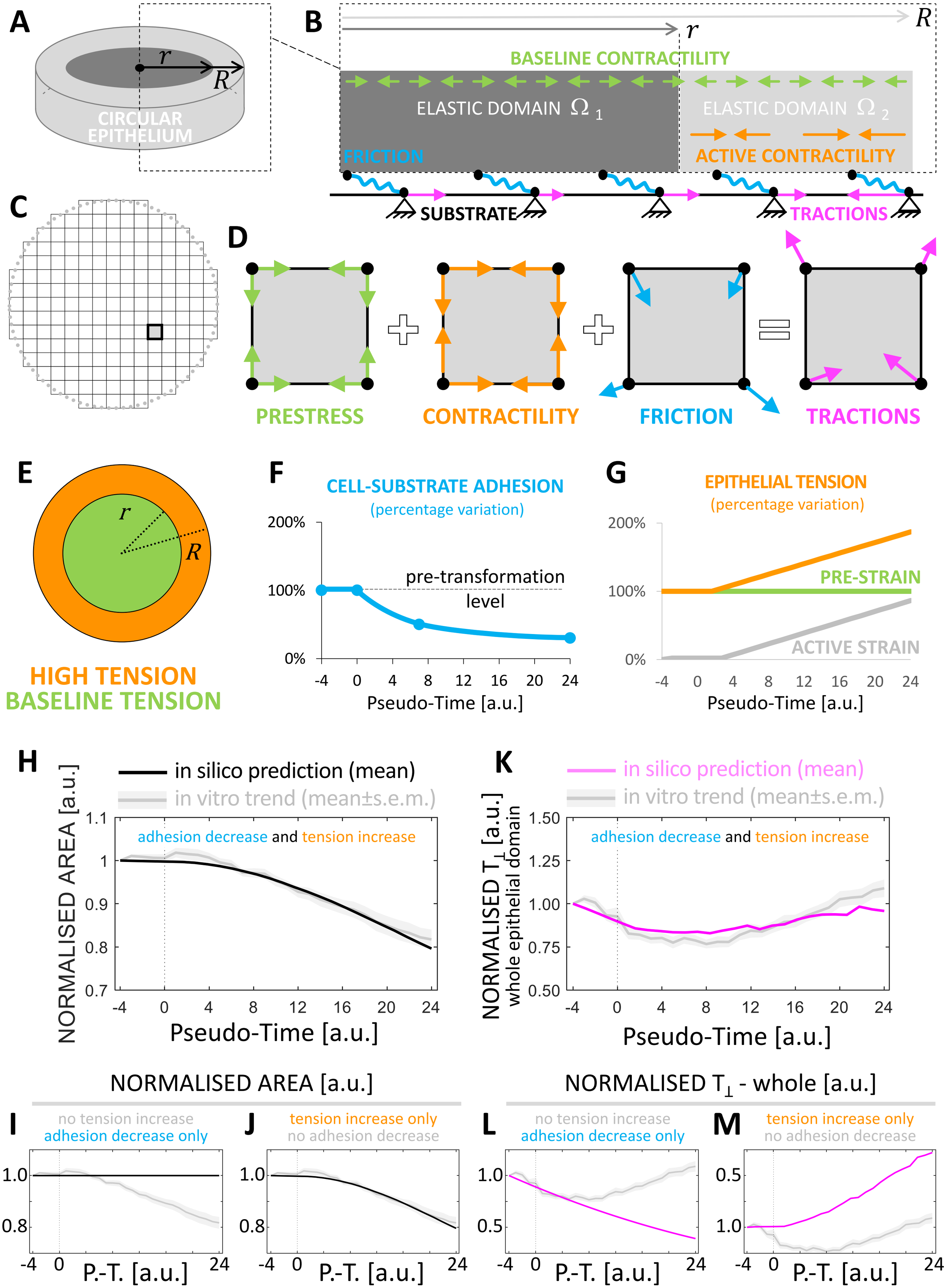
A
r
R
CIRCULAR EPITHELIUM
B
R
r
BASELINE CONTRACTILITY
ELASTIC DOMAIN Ω 1
ELASTIC DOMAIN Ω 2
FRICTION
ACTIVE CONTRACTILITY
SUBSTRATE
TRACTIONS
C
D
PRESTRESS
CONTRACTILITY
FRICTION
TRACTIONS
E
r
R
HIGH TENSION
BASELINE TENSION
F
CELL-SUBSTRATE ADHESION
(percentage variation)
200%
100%
0%
pre-transformation level
-4 0 4 8 12 16 20 24
Pseudo-Time [a.u.]
G
EPITHELIAL TENSION
(percentage variation)
200%
100%
0%
PRE-STRAIN
ACTIVE STRAIN
-4 0 4 8 12 16 20 24
Pseudo-Time [a.u.]
H
in silico prediction (mean)
in vitro trend (mean±s.e.m.)
NORMALISED AREA [a.u.]
adhesion decrease and tension increase
1.1
1
0.9
0.8
0.7
-4 0 4 8 12 16 20 24
Pseudo-Time [a.u.]
K
in silico prediction (mean)
in vitro trend (mean±s.e.m.)
NORMALISED T⊥ [a.u.]
whole epithelial domain
adhesion decrease and tension increase
1.50
1.25
1.00
0.75
0.50
-4 0 4 8 12 16 20 24
Pseudo-Time [a.u.]
NORMALISED AREA [a.u.]
NORMALISED T⊥ - whole [a.u.]
I
no tension increase
adhesion decrease only
1.0
0.8
-4 0 24
P.-T. [a.u.]
J
tension increase only
no adhesion decrease
1.0
0.8
-4 0 24
P.-T. [a.u.]
L
no tension increase
adhesion decrease only
1.0
0.5
-4 0 24
P.-T. [a.u.]
M
tension increase only
no adhesion decrease
0.5
1.0
-4 0 24
P.-T. [a.u.]

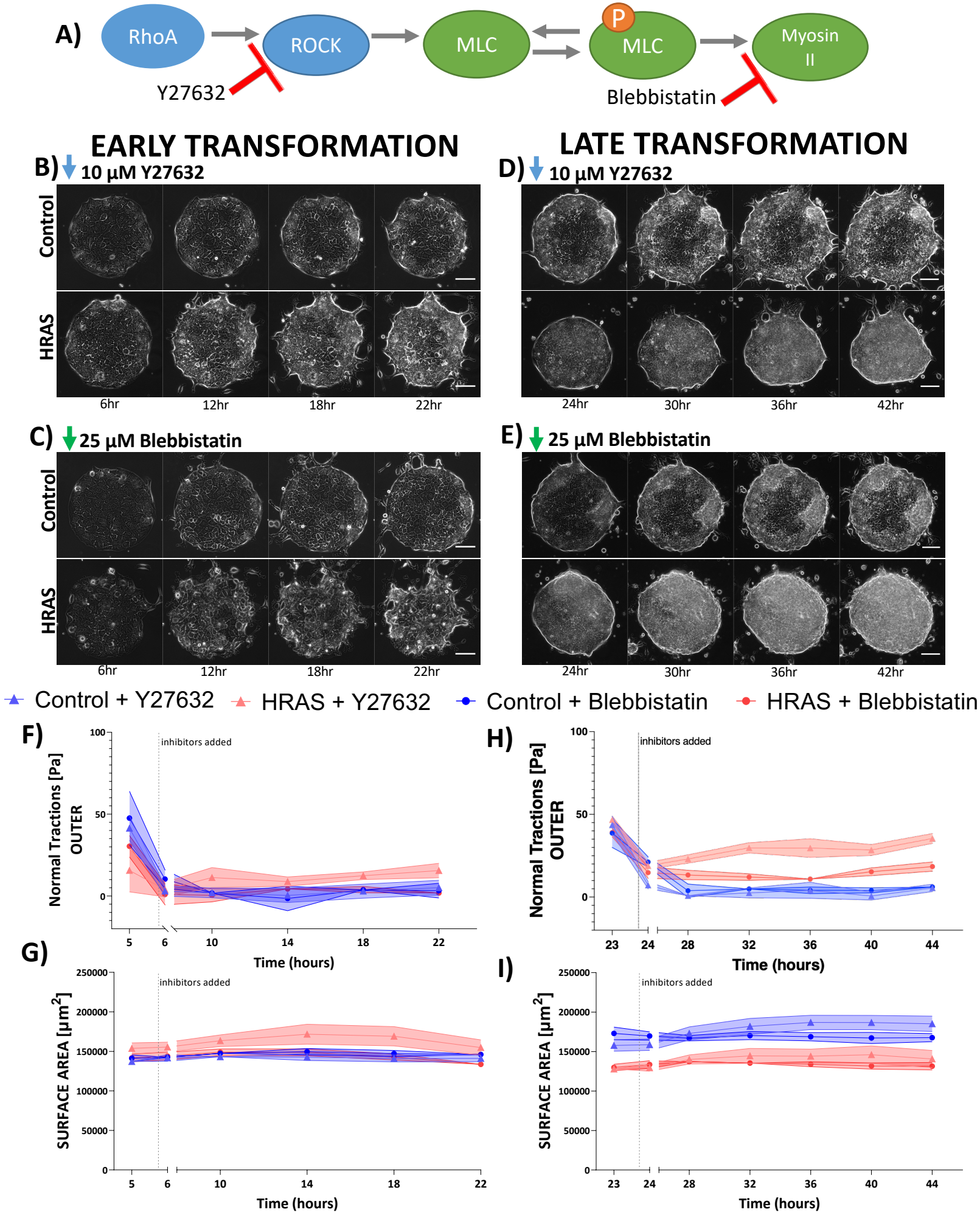
A)
RhoA
ROCK
MLC
P
MLC
Myosin II
Y27632
Blebbistatin
EARLY TRANSFORMATION
LATE TRANSFORMATION
B) 10 µM Y27632
D) 10 µM Y27632
Control
HRAS
6hr
12hr
18hr
22hr
24hr
30hr
36hr
42hr
C) 25 µM Blebbistatin
E) 25 µM Blebbistatin
Control + Y27632
HRAS + Y27632
Control + Blebbistatin
HRAS + Blebbistatin
F)
H)
Normal Tractions [Pa]
OUTER
inhibitors added
Time (hours)
G)
I)
SURFACE AREA [µm²]
inhibitors added
Time (hours)